HHS Public Access

Author manuscript

*Nature*. Author manuscript; available in PMC 2023 January 01.

Published in final edited form as:

*Nature*. 2022 July ; 607(7918): 321–329. doi:10.1038/s41586-022-04806-x.

# Targeting thalamic circuits rescues motor and mood deficits in PD mice

**Ying Zhang**[1,10], **Dheeraj S. Roy**[2,10], **Yi Zhu**[3], **Yefei Chen**[4,5], **Tomomi Aida**[1], **Yuanyuan Hou**[1], **Chenjie Shen**[1], **Nicholas E. Lea**[1], **Margaret E. Schroeder**[1], **Keith M. Skaggs**[1], **Heather A. Sullivan**[1], **Kyle B. Fischer**[6,7], **Edward M. Callaway**[6,7], **Ian R. Wickersham**[1], **Ji Dai**[4,5], **Xiao-Ming Li**[3,8,9], **Zhonghua Lu**[4,5], **Guoping Feng**[1,2]

[1]McGovern Institute for Brain Research, Department of Brain and Cognitive Sciences, Massachusetts Institute of Technology, Cambridge, MA, USA.

[2]Stanley Center for Psychiatric Research, Broad Institute of MIT and Harvard, Cambridge, MA, USA.

[3]Center for Neuroscience and Department of Neurology of Second Affiliated Hospital, Zhejiang University School of Medicine, Hangzhou, China.

[4]Shenzhen Key Laboratory for Molecular Biology of Neural Development, The Brain Cognition and Brain Disease Institute, Shenzhen Institutes of Advanced Technology, Chinese Academy of Sciences, Shenzhen, China.

[5]Shenzhen-Hong Kong Institute of Brain Science, Shenzhen, China.

[6]Systems Neurobiology Laboratories, Salk Institute for Biological Studies, La Jolla, CA, USA.

[7]Department of Neurosciences, University of California San Diego, La Jolla, CA, USA.

[8]NHC and CAMS Key Laboratory of Medical Neurobiology, Center for Brain Science and Brain-Inspired Intelligence, Guangdong-Hong Kong-Macao Greater Bay Area, Zhejiang University, Hangzhou, China.

[9]Joint Institute for Genetics and Genome Medicine between Zhejiang University and University of Toronto, Zhejiang University, Hangzhou, China.

[10]These authors contributed equally to this work.

## Summary



**Correspondence and requests for materials** should be addressed to Guoping Feng, Ying Zhang, or Dheeraj Roy. fengg@mit.edu, zhangyin@mit.edu, droy@broadinstitute.org.

Author contributions

Y.Z., D.R., and G.F. contributed to study design. Y.Z., D.R., T.A., C.S., M.S., and K.S. contributed to data collection and analysis. Y.Z., D.R., Y.H., and N.L. conducted surgeries and histological analyses. Y. Zhu and X.L. conducted all *in vivo* calcium imaging experiments. Y.C., J.D., and Z.L. conducted all macaque experiments. H.S. and I.W. provided all rabies viruses. K.F. and E.C. provided the anterograde HSV viruses. Y.Z., D.R., and G.F. wrote the paper. All authors discussed and commented on the manuscript.

Competing interests

The authors declare no competing interests, financial or otherwise.

Although bradykinesia, tremor, and rigidity are the hallmark motor defects in Parkinson's disease (PD) patients, they also experience motor learning impairments and non-motor symptoms such as depression[1]. The neural circuit basis for these different PD symptoms are not well understood. While current treatments are effective for locomotion deficits in PD[2,3], therapeutic strategies targeting motor learning deficits and non-motor symptoms are lacking[4–6]. We found that distinct parafascicular (PF) thalamic subpopulations project to caudate putamen (CPu), subthalamic nucleus (STN), and nucleus accumbens (NAc). While PF→CPu and PF→STN circuits are critical for locomotion and motor learning respectively, inhibition of the PF→NAc circuit induced a depression-like state. While chemogenetically manipulating CPu-projecting PF neurons led to a long-term restoration of locomotion, optogenetic long-term potentiation at PF→STN synapses restored motor learning behavior in PD model mice. Furthermore, activation of NAc-projecting PF neurons rescued depression-like PD phenotypes. Importantly, we identified nicotinic acetylcholine receptors capable of modulating PF circuits to rescue different PD phenotypes. Thus, targeting PF thalamic circuits may be an effective strategy for treating motor and non-motor deficits in PD.

Parkinson's disease (PD) is a neurodegenerative disorder characterized by the loss of dopamine neurons from substantia nigra pars compacta, abnormal activity in the basal ganglia network, and severe motor dysfunction[1]. PD motor symptoms such as rigor, tremor, and bradykinesia are treated by levodopa administration[2], or high frequency deep brain stimulation (DBS) targeting the subthalamic nucleus (STN) region[3]. PD patients also have motor learning impairments, specifically slower learning rates and retention deficits[4], which cannot be treated effectively[5]. In addition to motor symptoms, PD patients commonly experience debilitating non-motor phenotypes, including depression and anxiety[6], which have received limited attention. Identifying neural circuit mechanisms responsible for both motor and non-motor deficits in PD may lead to the development of novel therapeutic approaches. Parafascicular (PF) thalamus has extensive connectivity with the basal ganglia[7,8], critically contributes to motor behaviors[9,10], and PF DBS can modulate pathophysiological changes relevant to PD[11]. Based on these observations and the fact that PF thalamus projects to the nucleus accumbens (NAc)[12], a key structure involved in reward processing and depression-like behaviors[13], using male mice we systematically investigated the connectivity and function of PF inputs to basal ganglia nuclei as well as their relevance to motor and non-motor phenotypes in a PD model.

## Distinct subpopulations in PF thalamus

PF sends major projections to dorsal striatum (i.e., caudate putamen or CPu), STN, and ventral striatum (i.e., NAc)[12,14–16]. The physiological properties of these PF subpopulations and their circuits have not been extensively examined. We used both anterograde (Extended Data Fig. 1a, b) and retrograde (Extended Data Fig. 1c–f) tracing to confirm these three major projections. We found that retrograde cholera toxin subunit B (CTB) labeled CPu- or STN-projecting PF neurons ($PF_{CPu}$ or $PF_{STN}$) were intermingled in lateral PF, whereas NAc-projecting PF neurons ($PF_{NAc}$) were localized to medial PF (Fig. 1a). To determine whether the different PF subpopulations, in particular $PF_{CPu}$ and $PF_{STN}$ neurons, were part of the same ensemble or represent distinct ensembles, triple retrograde CTB tracing was

performed. Strikingly, there was minimal overlap between the three PF populations (Fig. 1b, Extended Data Fig. 1g–k).

*Ex vivo* electrophysiological recordings from retrograde rabies virus (RV) (dG-GFP)[17]-labeled PF neurons exhibited comparable basic electrophysiological properties between $PF_{CPu}$ and $PF_{STN}$ neurons, which were distinct from $PF_{NAc}$ neurons (Fig. 1c, Extended Data Fig. 1l–p). Light-evoked currents were larger in the PF→CPu and PF→NAc circuits as compared to PF→STN (Fig. 1d, and Extended Data Fig. 1q–s, 2a–c) and these circuits had different short-term plasticity (Extended Data Fig. 2d). Weaker currents of the PF→STN circuit were not due to a smaller ensemble size as compared to $PF_{CPu}$ and $PF_{NAc}$ neurons (Extended Data Fig. 1k) or any difference in the reliability across PF subpopulations (Extended Data Fig. 1r). These observations demonstrate that PF neurons projecting to CPu, STN, and NAc are distinct subpopulations.

## PF subpopulations mediate motor behavior

We first examined the role of PF subpopulations projecting to motor structures (i.e., CPu or STN). Using a retrograde RV-based approach[18], we observed robust projection-specific labeling (Fig. 2a). Compound 21 (C21)[19] reversibly inhibited hM4Di-expressing PF neurons *ex vivo* (Extended Data Fig. 2e). Although inhibition of $PF_{STN}$ neurons had no effect on locomotion, inhibition of $PF_{CPu}$ neurons resulted in a significant increase in motor activity (22.81% increase in $PF_{CPu}$ as compared to mCh controls) (Fig. 2b). The latter is different from a previous report[20] that employed chemogenetics to inhibit the entire PF and reported no significant change in behavior, suggesting that projection-specific PF manipulations may be more effective at revealing specific behavioral contributions. We next examined whether these PF subpopulations are involved in motor learning using a rotarod assay[21]. Consistent with the open field, $PF_{CPu}$ inhibited mice had a longer latency to fall on day 1 of rotarod as compared to control and $PF_{STN}$ inhibited mice (Extended Data Fig. 2f). Nevertheless, mCh and $PF_{CPu}$ inhibited mice showed significant enhancements in performance across days (30.36% and 17.75% increase in mCh and $PF_{CPu}$, respectively) (Fig. 2c), indicating effective motor learning. Although $PF_{STN}$ inhibited mice exhibited comparable performance on day 1 as control mice (Extended Data Fig. 2f), they lacked a learning-induced increase in performance across days (4.46% increase) (Fig. 2c). We measured the strength of distinct PF circuits before and after rotarod (Extended Data Fig. 2g). Rotarod training correlated with an increase in the AMPA/NMDA ratio of the PF→STN, but not PF→CPu, circuit (Fig. 2d, e). Optogenetic terminal inhibition in STN led to a decrease in rotarod-induced *cFos* in STN and showed that the PF→STN circuit is necessary for motor learning (Extended Data Fig. 2h–j). Therefore, while $PF_{CPu}$ neurons contribute to general motor activity, $PF_{STN}$ neurons are critical for motor learning, revealing differential functional roles of these two PF subpopulations.

To characterize the connectivity between PF and dopamine *D1* or *D2* receptor-expressing neurons in CPu[22], we used a Cre-dependent RV[23] system (Extended Data Fig. 2k, l). Both *D1* and *D2* neurons in CPu receive PF inputs (Extended Data Fig. 2m). *D1* and *D2* neurons in CPu had different neuronal excitability (Extended Data Fig. 2n), and we found that light-evoked currents were larger in *D1* as compared to *D2* neurons (Fig. 2f). It is widely

accepted that the major cell type in STN expresses a glutamatergic marker, *VGLUT2*[24,25]. However, STN also contains a parvalbumin (*PV*)-positive subpopulation[26,27], which remains understudied (Fig. 2g, Extended Data Fig. 2o). We found that a larger population of PF neurons projected to $PV^+$ STN neurons (Fig. 2h, Extended Data Fig. 3a–c), which was confirmed using *ex vivo* recordings (Fig. 2i). We hypothesized that $PV^+$ STN neurons may be crucial for motor learning. Inhibition of $PV^+$ or $VGLUT2^+$ STN neurons showed that only the *PV* inhibited group was impaired in motor learning (Fig. 2j, k, Extended Data Fig. 3d, e). Two additional experiments supported the role of $PV^+$ STN neurons in motor learning: inhibition of $VGLUT2^-$ neurons during behavior (Extended Data Fig. 3f), and inhibition of $PV^+$ STN neurons that receive PF inputs (Extended Data Fig. 3g).

We next compared the two STN cell types using *ex vivo* recordings (Extended Data Fig. 3h, i). Compared to $VGLUT2^+$ neurons, $PV^+$ neurons had action potentials with shorter half widths resulting in higher excitability (Fig. 2l, Extended Data Fig. 3j). Both STN populations had comparable spontaneous firing (Extended Data Fig. 3k), input resistance ($R_{in}$), membrane time constant (tau), membrane capacitance ($C_m$), and action potential amplitude (Extended Data Fig. 3l). *PV* neurons in the mammalian brain are usually inhibitory interneurons that regulate the output of neighboring excitatory neurons[28]. However, it has been shown that STN is devoid of the inhibitory neurotransmitter gamma-aminobutyric acid[29]. We found that the majority of $PV^+$ STN neurons expressed the excitatory glutamate transporter *VGLUT3* (Fig. 2m, Extended Data Fig. 3m). Recordings showed that $PV^+$ neurons did not exhibit local connectivity within STN (Extended Data Fig. 3n), which led to the hypothesis that these neurons are $PV^+$ excitatory, projection neurons. Indeed, anterograde tracing using a Cre-dependent HSV system (Fig. 2n, Extended Data Fig. 4a) or Cre-dependent ChR2-eYFP-expressing terminal labeling (Extended Data Fig. 4b, c), retrograde tracing (Extended Data Fig. 4d, e), and *ex vivo* recordings (Extended Data Fig. 4f–j) showed that these $PV^+$ STN neurons projected to GP and SNr[30]. Furthermore, using STN sections from macaques, we found that $PV^+$ neurons co-expressed *VGLUT3*, but not inhibitory glutamate decarboxylase 1/2 (Fig. 2o, Extended Data Fig. 4k). A retrograde virus injected in macaque SNr resulted in dense labeling in STN, many of which were $PV^+$ neurons (Fig. 2p). These experiments indicate that the excitatory projection $PV^+$ STN cell type is conserved from rodents to primates.

## PF→NAc neurons mediate depression

Using chemogenetics to inhibit $PF_{NAc}$ neurons (Fig. 3a), we found that this subpopulation does not play a critical role in the two motor assays that we employed (Fig. 3b, c, Extended Data Fig. 4l). Given that NAc plays a critical role in anxiety and depression[13], we tested $PF_{NAc}$ inhibited mice in the elevated zero maze (i.e., an anxiety assay) as well as three assays commonly used to detect depression-like states: sucrose preference test (SPT), forced swim test (FST), and tail suspension test (TST). While none of the three PF subpopulations played a role in anxiety (Fig. 3d), inhibition of $PF_{NAc}$ neurons led to a decrease in sucrose preference in SPT and an increase in immobility in both FST and TST, suggesting that this manipulation induces a depression-like state (14.75% decrease in SPT, 38.28% increase in FST, and 39.83% increase in TST of $PF_{NAc}$ relative to mCh) (Fig. 3e–g). To further support the role of $PF_{NAc}$ neurons in reward processing, we found that optogenetic activation of

these neurons induced real-time place preference, and that this population is necessary for cocaine-induced conditioned place preference but not a negative-valence contextual fear conditioning behavior (Extended Data Fig. 4m–p)[31]. These experiments revealed a crucial role for the $PF_{NAc}$ subpopulation in non-motor behaviors.

To strengthen the behavioral observations regarding distinct PF subpopulations, we performed *in vivo* physiological analyses using fiber photometry (Extended Data Fig. 4q). We observed an increase in the activity of $PF_{CPu}$ neurons, but not the other subpopulations, that started immediately before the onset of an immobility epoch in the open field, which was not the case before the end of immobility epochs (Fig. 3h, Extended Data Fig. 5a–f). Similarly, we observed a selective increase in the activity of $PF_{STN}$ neurons during the onset, but not the end, of the acceleration phase in the rotarod (Fig. 3i, Extended Data Fig. 5g–j, 6a–c). These observations were not a reflection of overall locomotion (Extended Data Fig. 5f, i, j, 6c). We also noted a selective increase in the activity of $PF_{NAc}$ neurons during the onset of struggling epochs in the TST along with a decrease in their activity before the end of struggling epochs (Fig. 3j, Extended Data Fig. 6d–f). The specificity of these observations was confirmed by imaging from the different PF subpopulations while simultaneously performing chemogenetic inhibition of the target subpopulation during behavior (Extended Data Fig. 6g–i). These experiments support the idea that PF contains at least three distinct functional subpopulations.

## Rescue of motor and non-motor PD defects

Because both motor and non-motor deficits are widely reported in PD[1,6], we tested whether manipulating PF circuits might have multiple therapeutic effects. PD mice were prepared by bilateral injections of 6-hydroxydopamine in substantia nigra pars compacta (SNc)[32], which led to the loss of dopaminergic cell bodies in SNc (Fig. 4a) and their terminals in CPu (Extended Data Fig. 7a); representing an acute PD model. As expected[33], PD mice exhibited a decrease in locomotion (Extended Data Fig. 7b). Inhibition of $PF_{CPu}$ neurons in wild type mice caused an increase in locomotion (Fig. 2b), suggesting that the physiological role of PF inputs to CPu is to decrease locomotion. Strength of the PF→CPu circuit was enhanced in PD mice (Extended Data Fig. 7c), which we hypothesized, may be responsible for the decreased locomotion in these animals. Inhibition of $PF_{CPu}$ neurons improved locomotion of PD mice, which was comparable to the level of control mice, when tested within an hour after C21 injections (Extended Data Fig. 7d–f)[20]. However, 3 days later, PD animals once again showed lower levels of locomotion compared to controls. We found that prolonged inhibition of $PF_{CPu}$ neurons for three days (Extended Data Fig. 7f) resulted in comparable levels of locomotion between control and PD mice both 7 and 10 days later (Fig. 4b, Extended Data Fig. 7g–j). Therefore, inhibition of $PF_{CPu}$ neurons offers an approach for the long-term rescue of locomotion defects in PD mice.

In addition to the locomotion phenotype in PD mice, we observed impairments in their motor learning (Fig. 4c)[33]. In contrast to wild type mice (Fig. 2e), PD mice lacked a learning-induced enhancement in the strength of the PF→STN circuit (Fig. 4d, Extended Data Fig. 8a), which correlated with the lack of rotarod-induced *cFos* in STN (Extended Data Fig. 8b). We thought that strengthening the PF→STN circuit might rescue this

phenotype. To test this idea, we employed an *in vivo* optical long-term potentiation (LTP) approach for circuit strengthening, which activated neurons at 100 Hz using *oChIEF*[34,35]. We activated PF terminals in STN using three different protocols (Extended Data Fig. 8c, d). To determine whether increasing PF→STN activity during rotarod trials or strengthening the PF→STN circuit between trials is sufficient to rescue motor learning, we tested 20 Hz stimulation during rotarod or 100 Hz stimulation between trials. Since neither improved motor learning in PD mice (Extended Data Fig. 8e), we activated the PF→STN circuit using a combination of 20 Hz and 100 Hz protocols (20 + 100 Hz, hereafter referred to as optical LTP). Optical LTP applied to the PF→STN circuit rescued motor learning (Fig. 4c), and led to a learning-induced circuit strengthening (Fig. 4d) together with significant STN *cFos* (Extended Data Fig. 8f). Inhibition of $PV^+$ STN neurons prevented this LTP-based rescue (Extended Data Fig. 8g, h), which directly demonstrated the crucial role of $PV^+$ STN neurons in this rescue approach.

We next investigated a common non-motor deficit in PD, specifically depression[6]. PD mice showed decreased preference in SPT (Extended Data Fig. 8i), along with increased immobility in both FST and TST (Extended Data Fig. 8j), indicating a depression-like state. Similar to the PF→CPu circuit, both *D1* and *D2* neurons in NAc receive PF inputs (Extended Data Fig. 8k–m), *D1* and *D2* neurons in NAc show distinct excitability (Extended Data Fig. 8n), and light-evoked currents *ex vivo* are larger in *D1* neurons (Fig. 4e). PD mice showed a decrease in the response of *D1* neurons to PF inputs *ex vivo*, while *D2* responses were unaffected (Fig. 4e). We speculated that increasing $PF_{NAc}$ activity during behavior might be sufficient to rescue PD phenotypes. Taking into account the FST and TST protocols, we believed that a minimally invasive neuronal manipulation method would be preferred, which is why we employed our recently developed stable step-function opsin SOUL[36]. This opsin expressed in the mouse brain can be activated by a brief light stimulation from outside the skull[36]. We generated a Cre-dependent SOUL virus and verified $PF_{NAc}$ labeling (Fig. 4f), and validated our ability to depolarize these neurons (Fig. 4g, Extended Data Fig. 8o). Activating $PF_{NAc}$ neurons in PD mice improved performance in all three assays used to detect depression-like states (Fig. 4h). Therefore, modulating PF circuits is an effective approach to rescue motor and non-motor deficits in PD mice.

## Targeting PF nAChRs rescues PD defects

Since strengthening PF inputs to $PV^+$ STN neurons optogenetically was sufficient for behavioral rescue in PD mice, we wanted to determine whether a similar effect might be achieved using a molecular target. We used two criteria to identify molecular target candidates: a) these molecules are capable of modulating synaptic plasticity in multiple brain regions based on the literature, and b) these molecules are expressed in STN (Extended Data Fig. 9a)[37]. Following these criteria, we narrowed down to $\alpha 7$ nicotinic acetylcholine receptors (nAChRs)[38], nitric oxide (*NO*) receptor *GUCD1*[39], *ERBB4* receptor[40], and μ-opioid receptor *OPRM1*[41]. We tested whether modulating these candidate molecular targets *ex vivo* could enhance synaptic plasticity in the PF→STN circuit of PD mice. We established a baseline condition in which the PF→STN circuit from PD mice did not exhibit an increase in synaptic strength following optical high frequency stimulation (HFS) (Extended Data Fig. 9b). Although a *NO* receptor agonist, an *ERBB4* receptor antagonist,

and a μ-opioid receptor agonist failed to strengthen this circuit (Extended Data Fig. 9c), an *α7* nAChR agonist, PNU282987[42], resulted in an increase in the AMPA/NMDA ratio after HFS (Extended Data Fig. 9d). We directly showed that *PV*$^+$ STN neurons highly expressed *α7* nAChRs (Fig. 5a). When we performed rotarod training in PD mice injected with PNU282987, we detected an increase in the synaptic strength of PF inputs to *PV*$^+$ STN neurons *ex vivo* (Fig. 5b), which was accompanied by a significant improvement in motor learning (Fig. 5c, Extended Data Fig. 9e). This PNU282987-induced rescue of motor learning was blocked by simultaneous chemogenetic inhibition of *PV*$^+$ STN neurons, suggesting that activation of *α7* nAChRs specifically in *PV*$^+$ STN neurons is necessary for behavioral rescue in PD mice (Fig. 5c). This idea was supported by performing a CRISPR/Cas9-based *in vivo* knockdown (KD)[43] of *α7* nAChRs from *PV*$^+$ STN neurons specifically, which blocked the motor learning rescue effect of PNU282987 in PD mice (Extended Data Fig. 9f, g).

It has been reported that the knockdown of a different nAChR, *α6*, in PF alleviates certain motor phenotypes in PD mice[44]. Consistent with this study, using an *α6* nAChR antagonist[45], we found that this manipulation brings down the strength of the PF→CPu circuit in PD mice *ex vivo* (Fig. 5d). We observed that *α6* nAChRs are enriched in $PF_{CPu}$ neurons but are not expressed by *D1* or *D2* MSNs in CPu (Extended Data Fig. 9h), suggesting that *α6* nAChRs modulate the PF→CPu circuit using a presynaptic mechanism. Local infusions of the *α6* nAChR antagonist in CPu of PD mice rescued their locomotion deficit (Fig. 5e, Extended Data Fig. 9i). Similarly, when we performed a circuit-based *in vivo* KD[43] of *α6* nAChRs selectively from $PF_{CPu}$ neurons in PD mice, we rescued their locomotion deficit (Extended Data Fig. 9j, k). These findings suggested that targeting nAChRs in different PF circuits is sufficient to rescue motor phenotypes in PD mice.
To extend this approach to the PF→NAc circuit, we identified several nAChRs (i.e., *α3*, *α6*, *α7*, and *β2*) expressed in PF and NAc according to the Allen Brain Atlas in situ hybridization database[37]. Using agonists for each of these nAChRs, recordings showed that modulating *β2* nAChRs increases the strength of PF inputs to *D1* neurons in NAc (Fig. 5f, Extended Data Fig. 10a). Complementing this observation, *β2* nAChRs are enriched in *D1* NAc neurons as compared to *D2* NAc neurons (Fig. 5g). Local infusions of the *β2* nAChR agonist in NAc of PD mice led to improved performance in all three assays of depression-like behaviors (Fig. 5h, Extended Data Fig. 10b). Also, selective KD of *β2* nAChRs in *D1*$^+$ NAc neurons blocked the rescue effect of the *β2* nAChR agonist, further strengthening our observations (Extended Data Fig. 10c, d). Similar to mice, using macaque tissue we found that *α7* nAChRs are highly expressed in *PV*$^+$ STN neurons, *α6* nAChRs are expressed in PF neurons, and *β2* nAChRs are highly expressed in *D1*$^+$ NAc neurons (Fig. 5i). Together, these data suggest that targeting different nAChRs in PF circuits may offer a potential therapeutic approach to alleviate both motor and non-motor deficits in PD.

## Discussion

Interest in PF thalamus initially came from anatomical studies showing extensive connectivity with the basal ganglia network[7,8]. It has since been shown that PF contributes to motor tasks such as reversal learning and movement sequences, which is thought to arise from its projections to CPu[9,10]. Although heterogeneity within PF has been suggested[46,47],

whether distinct circuits underlie different motor behaviors remains understudied. Also, the potential role of PF's projections to NAc[12] has not been revealed. Here, to our knowledge, we have shown for the first time that PF neurons projecting to CPu, STN, and NAc are distinct subpopulations and have differential functional relevance: motor behaviors (PF→CPu and PF→STN) vs. non-motor behaviors (PF→NAc). While NAc-projecting neurons are restricted to medial PF, CPu- and STN-projecting neurons can be found intermingled mostly in lateral PF, indicating differences in the spatial localization of PF subpopulations. Among these three subpopulations, NAc-projecting PF neurons exhibit the most unique electrophysiological profile. We noted that both *D1* and *D2* neurons in NAc receive PF inputs, similar to *D1*/*D2* neurons in CPu. Intriguingly, in both NAc and CPu, *D2* neurons exhibited higher *ex vivo* excitability as compared to *D1*. Classical models suggest that these cell types support differential functions in NAc (*D1* for reward, *D2* for aversion)[48] and CPu (*D1* to promote movement, *D2* to inhibit movement)[49]. Because in both NAc and CPu *D2* neurons are recruited to regulate reward or movement behavior, it may be essential for this cell type to be more excitable and thus be more responsive to small changes in incoming synaptic inputs.

Similar to PD patients[1,4], mouse models of PD have impairments in both locomotion and motor learning, which were rescued by manipulating CPu- and STN-projecting PF subpopulations in the same mice (Extended Data Fig. 10e–g). With regards to the rescue of locomotion in PD model mice, acute manipulations of $PF_{CPu}$ neurons improved behavioral performance immediately, consistent with a previous report[20]. However, we found that this rescue was not long lasting, which was not examined by the previous study[20]. We made a surprising finding that a prolonged manipulation protocol resulted in a long lasting rescue of locomotion in PD model mice (up to 10 days later). A recent study showed that distinct PF subpopulations project to CPu vs. STN[50], consistent with our results, and found that the activation of the PF→STN circuit, but not the PF→CPu circuit, increases locomotion. While these behavioral observations suggest differential functions of these PF circuits, the function of the PF→CPu circuit was not revealed, and importantly, different from our study, the authors did not employ loss-of-function manipulations to identify the physiological role of these circuits in behavior. Therefore, our work using loss-of-function experiments led to the identification of new functions for the different PF circuits. This recent study[50] also showed that the activation (using 5–40 Hz stimulation protocols) of the PF→STN circuit in PD mice is sufficient to rescue locomotion and a variety of natural behaviors. In the present study, because we found that the PF→STN circuit is necessary for motor learning, but not locomotion, and that this circuit is weakened in PD model mice, we employed an optical LTP protocol (~100 HZ) to strengthen this circuit and restore motor learning behavior. Together, these observations suggest that the activation of the PF→STN circuit, depending on the stimulation parameters used, may alleviate both locomotion and motor learning deficits in PD.

In addition to motor phenotypes, PD patients experience severe non-motor symptoms including depression[6], which can also be observed in PD mice. Using a minimally invasive optogenetic approach[36] to modulate $PF_{NAc}$ neurons, we demonstrated that activating this specific PF subpopulation in PD mice is sufficient to alleviate depression-like behaviors. Because these findings are based exclusively on male mice and sex differences are

well documented in PD, future research is needed to determine whether these circuit manipulations are equally effective in female mice. This is particularly important for the rescue of depression-like behaviors, which is a severe mood disorder that is approximately twice as prevalent in women as compared to men. Nevertheless, our observations highlight the importance of heterogeneous PF neurons to behavior, in both normal and disease states, and suggests that both motor and non-motor PD deficits may be treated by targeting PF thalamic circuits.

Although levodopa and STN DBS are effective treatments for a range of motor symptoms in PD, slower motor learning and subsequent retention deficits do not respond well to these approaches[5]. In this study, we demonstrated that strengthening the PF→STN circuit in PD mice was sufficient to restore long-term motor learning. Further experiments aimed at understanding the cellular basis of this rescue in PD mice revealed that a $PV^+$ excitatory STN cell type was crucial. This observation suggests that STN, although generally considered to be homogeneous, contains distinct functional subpopulations[25]. In addition to our experiments showing that selective strengthening of PF inputs to $PV^+$ STN neurons can rescue motor learning deficits, we showed that the majority of $PV^+$ STN neurons express $\alpha 7$ nAChRs, which if activated in PD mice using an agonist led to the rescue of motor learning deficits in a $PV^+$ STN neuron-dependent manner. Because we found that STN of macaques also contain excitatory projection $PV^+$ neurons that co-express $\alpha 7$ nAChRs and previous work has reported the presence of $PV^+$ STN neurons in human samples[30], our mechanistic findings in rodent STN may be conserved in higher species such as non-human primates and even in humans.

Finally, we wanted to identify molecular targets that are capable of modulating the three different PF circuits. Similar to our PF→STN $\alpha 7$ nAChR experiments, another group reported that modulating $\alpha 6$ nAChRs in PF improves certain motor behaviors[44]. Building on their work, we showed that an $\alpha 6$ nAChR antagonist targeting $PF_{CPu}$ neurons rescues locomotion. Furthermore, we found that PF inputs to *D1* neurons in NAc are selectively weakened in PD mice. Using a $\beta 2$ nAChR agonist, we were able to rescue the strength of PF inputs to NAc $D1^+$ neurons in PD mice and their depression-like behavioral deficits. Together, we not only identified circuit mechanisms responsible for motor and non-motor deficits in PD mice, but also propose that using nAChRs capable of regulating three distinct PF circuits offers an exciting therapeutic avenue for PD.

## Methods

### Subjects

**Mice.—**C57BL/6J wild type, Vglut2-Cre (Stock No. 028863), PV-Cre (Stock No. 017320), D2-eGFP (Stock No. 030255), PV-Flp (Stock No. 022730), and D1-Cre (Stock No. 030329) mice were obtained from Jackson Laboratory. D2-Cre (i.e., Drd2-Cre) mice were imported from the GENSAT Project at Rockefeller University. All mice were housed in a 7 am-7pm light on-off cycle facility with a temperature of 18–23 degrees C and humidity maintained between 40–60%. Food and water were available *ad libitum*. Adult mice were housed in groups (2 to 5 animals per cage) before surgery. Following surgery, mice were single housed. Male mice at 9–20 weeks of age were used for all experiments. All experimental procedures

were conducted in accordance with the U.S. National Institutes of Health (NIH) guidelines and the Massachusetts Institute of Technology Department of Comparative Medicine and Committee of Animal Care.

**Monkeys.—**Cynomolgus monkeys (*Macaca fascicularis*) (male, 2–3 years old, weight 2.0–2.3 kg) were housed in an environmentally controlled facility (temperature: 22 ± 1°C, humidity: 50 ± 5% relative humidity). All monkeys were fed with commercial monkey food twice per day, plus one meal of seasonal fruits daily, and had free access to water. Monkeys were under careful veterinary monitoring twice per day to evaluate and ensure their health status. The primate facility used was accredited by the Association for Assessment and Accreditation of Laboratory Animal Care (AAALAC) and therefore followed their guidelines closely.

## Fluorescent in situ hybridization (FISH) in mice

Mouse brain samples were carefully extracted, embedded in OCT compound (Tissue-Tek), and flash frozen. Coronal sections (16 μm thickness) were prepared on a cryostat (Leica) and stored at −80°C until staining. ACD RNAScope multiplex fluorescent protocol was applied for mRNA FISH staining using fresh frozen tissues. Briefly, charged slides with slices were fixed in pre-chilled paraformaldehyde (PFA) for 30 min, followed by a series of dehydration steps using 50%, 70%, and 100% ethanol. Sections were then permeabilized with ACD protease IV for 30 min, followed by probe hybridization for 2 hr at 40°C. Fluorescent labeling of up to 3 probes per section was performed using four steps of Amp 1-FL to Amp 4-FL. Sections were stained with DAPI and stored at 4°C. Mouse ACD probes for *Slc17a6/Vglut2* (Cat. No. 319171), *PV* (Cat. No. 421931), *GFP* (Cat. No. 409011), *mCh* (Cat. No. 431201), *eYFP* (Cat. No. 312131), *Chrna7* (Cat. No. 465161), *Chrna6* (Cat. No. 467711), *Slc17a8/Vglut3* (Cat. No. 431261), *Chrnb2* (Cat. No. 449231), *Drd1/D1* (Cat. No. 406491), *Drd2/D2* (Cat. No. 406501), *Oprm1* (Cat. No. 315841), *Gucd1* (Cat. No. 870431), and *ErbB4* (Cat. No. 318721) were used. To elevate *Vglut2*, *PV*, and *Vglut3* signal in neuronal cell bodies, mice were treated with an intracerebroventricular injection of colchicine (6 μg in 1 μl, Sigma) 48 hr before tissue collection. Stained sections were imaged with a 20X magnification objective on a Leica confocal microscope.

## FISH in macaque

Coding region fragments of macaque *Gad1, Gad2, Vglut3, Chrna7*, *Chrna6*, *Chrnb2*, and dopamine receptor *D1* were isolated from monkey brain cDNA using PCR amplification. The amplified fragments were cloned into the pCR4 Topo vector (Thermo Fisher). Hybridization was performed as previously described with minor modifications[51]. Briefly, digoxigenin (DIG)-labeled cRNA probes (riboprobes) were prepared using the DIG RNA labeling mix (Roche). Brains were frozen in OCT (Tissue-Tek), and coronal cryostat sections of 50 μm thickness were hybridized to DIG-labeled cRNA probes at 56°C for 15–18 hr. After hybridization, sections were washed twice in 0.2x SSC at 62°C for 30 min, incubated with peroxidase (POD)-conjugated anti-DIG antibodies (1:500, Roche, Cat. No. 1207733910) at 37°C for 2 hr, and then treated with the TSA-plus kit (Perkin Elmer).

### Immunohistochemistry (IHC) in mice

Mice were anesthetized with isoflurane and transcardially perfused with phosphate buffered saline (PBS), followed by 4% PFA. Brains were extracted and post-fixed with 4% PFA overnight. Next, brains were transferred to PBS and sectioned into 50 μm coronal sections using a vibratome. Sections were stored at 4°C in PBS until they were processed. For IHC, free-floating sections were washed with PBS three times (5 min each) and incubated with blocking buffer that contained 5% normal goat serum dissolved in 0.2% PBST (0.2% Triton X-100 in PBS) for 1 hr. Sections were then incubated with primary antibody (diluted in blocking buffer) overnight at 4°C. After primary, sections were washed three times (10 min each) with PBST, followed by a 2 hr incubation with the secondary antibody. After three washes (10 min each) with PBST, sections were transferred onto charged Super Frost slides, and mounted under glass coverslips with mounting media. Tyramide signal amplification (TSA)-IHC protocol was applied for STN and PF cFos staining experiments. Following primary antibody incubation as described above, sections were introduced to a secondary antibody working solution (Opal Polymer HRP Ms + Rb in blocking/Ab diluent, 1:100) for 30 min at room temperature. After three washes (10 min each) with PBST, sections were transferred to a TSA Plus working solution (Opal 520 or Opal 570 in 1x plus amplification diluent, 1:100) for 15 min at room temperature. After three more wash steps of 15 min each in PBST, slices were mounted on microscope slides and imaged with a 20X magnification objective on a Leica confocal microscope. Antibodies used for staining were as follows: chicken anti-GFP (1:1000, Life Technologies) and anti-chicken Alexa-488 (1:1000), rabbit anti-RFP (1:1000, Rockland) and anti-rabbit Alexa-555 (1:500), mouse anti-NEUN (1:200, Millipore) and anti-mouse Alexa-555 (1:500), mouse anti-TH (1:1000, Immunostar) and anti-mouse Alexa-488 (1:500), rabbit anti-cFos (1:500, Cell Signaling Technology), and all nuclei were stained with DAPI (1:3000, Sigma) shown in the blue channel. To elevate *cFos* signal in STN neuronal cell bodies, mice were treated with an intracerebroventricular injection of colchicine (6 μg in 1 μl, Sigma) 48 hr before behavior and perfusion fixation.

### Cell counting in mice

Images were processed using ImageJ, and final quantifications were performed manually from 3–5 sections per animal. Counting experiments were conducted blind to experimental group where Researcher 1 prepared slices and performed staining experiments, while Researcher 2 performed quantification analyses. For experiments using virus-injected mice, Researcher 1 started by verifying accurate viral targeting and only those samples that passed this checkpoint were included in further analyses. For each fluorescence channel, a threshold was carefully determined in ImageJ that permitted the automatic identification of putative fluorescently labeled neurons across 2–3 slices from at least 3 mice per experiment. This process allowed for a standardization of the fluorescence intensity threshold per channel. Because this automatic identification often labeled a single neuron with several maxima, it was necessary to use visual inspection and perform manual cell counting in order to obtain the most accurate number of neurons expressing each target protein. This approach was also used to quantify co-expression of multiple fluorescent proteins. To quantify the chance level at which retrograde tracing of CPu, STN or NAc using CTB results in non-overlapping PF populations, we performed *NEUN* staining and found that 35.99% of PF neurons project to CPu, 30.11% of PF neurons project to STN, and 18.52% of PF neurons project to NAc.

Assuming the projections from PF to downstream nuclei arise from distinct populations, chance level for PF neurons that project to CPu only was calculated as 0.3599 × (1–0.3011) × (1–0.1852) = 0.2049, chance level for PF neurons that project to STN only was calculated as 0.3011 × (1–0.3599) × (1–0.1852) = 0.157, and chance level for PF neurons that project to NAc only was calculated as 0.1852 × (1–0.3599) × (1–0.3011) = 0.0828.

## IHC in macaque

Animals were deeply anesthetized with sodium pentobarbital (nembutal; 80 mg/kg, i.p.) and perfused with PBS (0.1 M) and 4% paraformaldehyde in PBS (4% PFA/PBS, 4°C, 500 ml). The dissected brains were post-fixed at 4°C in 4% PFA/PBS and cryo-protected at 4°C in 30% sucrose/PBS. Coronal sections (50 μm) were prepared using a vibrating blade microtome (Leica, CM1950). All sections were post-fixed for 20 min at 4°C in 4% PFA/PBS. Sections were blocked and permeabilized for 1 hour at room temperature in a PBS solution containing 5% bovine serum albumin (BSA) and 0.3% Triton X-100. The primary antibody incubation was performed by incubating the sections overnight at 4°C in a PBS solution containing 5% BSA, polyclonal anti-RFP (1:500, Rockland, Cat. No. 600-401-379), and anti-PV (1:500, Swant, Cat. No. 235). The secondary antibody incubation was performed for 1 hr using Alexa Fluor 594 donkey anti-rabbit IgG and Alexa Fluor 488 donkey anti-mouse IgG (1:500, Thermo Fisher Cat. No. A32754 and Cat. No. A21202, respectively). Nuclei were stained with DAPI (Sigma-Aldrich, Cat. No. D9542) shown in the blue channel. Brain sections were mounted onto slides using Fluoromount-G mounting medium (SouthernBiotech, Cat. No. 0100–01).

## Cell counting in macaque

Images were acquired using a confocal microscope (LSM 800, Carl Zeiss) with a 20X magnification objective. Brain structures were identified microscopically and in digital photos using a monkey brain atlas. Quantifications were performed from 3 macaques. Three slices form rostral to caudal STN were analyzed. Cell counting was done in ImageJ, and all measurements were made independently and blindly.

## Virus preparation

$AAV_9$-EF1α-DIO-ChR2-eYFP (catalog #20298, $7 \times 10^{12}$ GC $ml^{-1}$ viral titer), $AAV_9$-CaMKII-ChR2-eYFP (catalog #26969, $1 \times 10^{13}$ GC $ml^{-1}$ viral titer), $AAV_9$-CaMKII-ChR2-mCherry (catalog #26975, $7 \times 10^{12}$ GC $ml^{-1}$ viral titer), $AAV_8$-hSyn-DIO-hM4Di-mCherry (catalog #44362, $1 \times 10^{13}$ GC $ml^{-1}$ viral titer), $AAV_8$-hSyn-DIO-mCherry (catalog #50459, $7 \times 10^{12}$ GC $ml^{-1}$ viral titer), $AAV_1$-hSyn-Cre (catalog #105553, $1 \times 10^{13}$ GC $ml^{-1}$ viral titer), $AAV_8$-EF1α-COn/FOn-NpHR3.3-eYFP (catalog #137152, $1 \times 10^{13}$ GC $ml^{-1}$ viral titer), $AAV_8$-hSyn-COn/FOn-eYFP (catalog #55650, $1 \times 10^{13}$ GC $ml^{-1}$ viral titer), AAVretro-hSyn-Cre (catalog #105553, $7 \times 10^{12}$ GC $ml^{-1}$ viral titer), $AAV_9$-Syn-DIO-GCaMP6s (catalog #100845, $1 \times 10^{13}$ GC $ml^{-1}$ viral titer), and $AAV_8$-DIO-hM4Di-mCitrine (catalog #50455, $1 \times 10^{13}$ GC $ml^{-1}$ viral titer) viruses were purchased from Addgene. AAV constructs for $AAV_8$-CaMKII-eYFP (plasmid #105622), $AAV_9$-EF1α-DIO-ChR2-mCherry (plasmid #35508), $AAV_8$-EF1α-DO-NpHR3.0-eYFP (plasmid #37087), $AAV_8$-EF1α-DO-eYFP (plasmid #37085), $AAV_8$-CaMKII-oChIEF-mCherry (plasmid #51092), and $AAV_8$-Syn-oChIEF-mCherry (plasmid #50977) were obtained from Addgene and packaged by the

Viral Core at Boston Children's Hospital (~$3 \times 10^{13}$ GC $ml^{-1}$ viral titer). $AAV_8$-CaMKII-eArch3.0-eYFP virus ($8 \times 10^{12}$ GC $ml^{-1}$ viral titer), $AAV_8$-EF1α-DIO-eArch3.0-eYFP ($1.6 \times 10^{13}$ GC $ml^{-1}$ viral titer), and $AAV_9$-EF1α-DIO-eYFP ($2 \times 10^{13}$ GC $ml^{-1}$ viral titer) were acquired from the University of North Carolina (UNC) at Chapel Hill Vector Core. For Cre-dependent anterograde circuit tracing, helper virus (AAV8-nef-DIO-mCherry-p2a-coUL6, $4.33 \times 10^{13}$ GC $ml^{-1}$) and HSV virus (HSV-H129-LSL-TK-GFP dUL6, $3.8 \times 10^{13}$ pfu $ml^{-1}$) were used. We generated the $AAV_9$-EF1α-DIO-SOUL-tdTomato construct and packaged this virus at the Boston Children's Hospital Viral Core ($1 \times 10^{13}$ GC $ml^{-1}$ viral titer). For rabies virus-mediated transneuronal labeling, pAAV-Syn-FLEX-splitTVA-EGFP-tTA (Addgene catalog #100798) and pAAV-TREtight-mTagBFP2-B19G (Addgene catalog #100799)[52] were packaged in serotype 1 AAV capsids by the UNC Vector Core, with titers $8.48 \times 10^{11}$ GC $ml^{-1}$ and $6.50 \times 10^{11}$ GC $ml^{-1}$, respectively, and combined in a 1:1 ratio by volume before injections, G-deleted EnvA-rabies-mCherry ($8 \times 10^9$ GC $ml^{-1}$ viral titer), G-deleted, mCherry-expressing rabies virus (RV-dG-mCherry, $7 \times 10^9$ GC $ml^{-1}$ viral titer), G-deleted, GFP-expressing rabies virus (RV-dG-GFP, $7 \times 10^9$ GC $ml^{-1}$ viral titer), and GL-deleted, Cre-expressing rabies virus (dGL-Cre, $8 \times 10^9$ GC $ml^{-1}$ viral titer) were provided by Ian Wickersham's lab at Massachusetts Institute of Technology.

## Mouse surgery

Mice were anesthetized with isoflurane for stereotaxic injections. 1 mg $kg^{-1}$ meloxicam was given as analgesic prior to incisions. Viral vectors, cholera toxin (CTB), nAChR modulators, or colchicine were injected with a glass pipette at a flow rate of 70 nl $min^{-1}$. The pipette was withdrawn 10 min after the end of the injection. For optic fiber implantation, single 200 μm fiber implants (Newdoon) were placed either above injection sites or terminals, and secured to the skull with two jewelry screws, adhesive cement (C&B Metabond), and dental cement. Mice were given 1–2 mg $kg^{-1}$ sustained-release buprenorphine as analgesic after surgeries and allowed to recover for at least 2 weeks before behavioral experiments. All injection sites were verified histologically. As criteria, we only included mice with virus expression and fiber implantations limited to the targeted regions. Stereotaxic coordinates for injections/implantations were: PF (300 nl): anteroposterior (AP) −2.18 mm, mediolateral (ML) +/− 0.7 mm, dorsoventral (DV) −3.25 mm, CPu (400 nl): AP 0.3 mm, ML +/− 2.5 mm, DV −3.25 mm, STN (300 nl): AP −1.56 mm, ML +/− 1.4 mm, DV −4.8 mm, NAc (250 nl): AP 1.1 mm, ML +/− 1.25 mm, DV −4.3 mm, GP (350 nl): AP −0.46 mm, ML +/− 1.9 mm, DV −4 mm, and SNr (380 nl): AP −3.08 mm, ML +/− 1.5 mm, DV −4.8 mm. For three-site CPu injections, coordinates were: $CPu_1$ (350 nl): AP 1.34 mm, ML +/− 1.5 mm, DV −3.25 mm, $CPu_2$ (350 nl): AP 0.62 mm, ML +/− 1.75 mm, DV −3.5 mm, and $CPu_3$ (350 nl): AP 0.3 mm, ML +/− 2.5 mm, DV −3.25 mm. For intracerebroventricular injection of colchicine (400 nl), the target coordinate was: AP −1.56 mm, ML +/− 2.5 mm, DV −4 mm. To characterize neuronal populations of PF based on downstream projection targets, we used CTB conjugated to Alexa-488, Alexa-555, or Alexa-633 diluted in PBS at a final concentration of 1% wt $vol^{-1}$. Mice were perfused for histology six days after CTB injections. For tracing experiments using different Cre mouse lines, AAV-$FLEX^{loxP}$-TVA-GFP-Rabies glycoprotein was injected unilaterally in CPu, STN, or NAc. One week later, G-deleted EnvA-rabies-mCherry was injected in CPu, STN, or NAc at the same coordinates. Six days after the second virus injection, mice were perfused for histology and

imaging. Neurons that expressed both GFP (from helper virus) and mCherry (from rabies virus) were defined as starter cells. To label $PF_{CPu}$, $PF_{STN,}$ and $PF_{NAc}$ neurons for *ex vivo* recordings, RV-dG-GFP was injected in CPu, STN, or NAc, respectively. Slice recordings were performed 4 days after injections. For DREADDs-based neuronal inhibition during behavior, PF subpopulations were labeled by injecting a retrograde RVdGL-Cre virus in CPu, STN, or NAc combined with a Cre-dependent hM4Di-mCherry virus in PF. mCherry (mCh) control mice received a Cre-dependent mCherry virus in PF in place of the hM4Di virus. DREADDs-based inhibition of $PV^+/VGLUT2^+$ STN neurons used a Cre-dependent hM4Di virus injected into STN of Vglut2-Cre or PV-Cre mice. For *ex vivo* recordings from *D1*/*D2* MSNs in CPu that receive PF input, ChR2-mCherry virus was injected in PF of D2-eGFP mice. For *ex vivo* recordings from *PV*/*VGLUT2* in STN that receive PF input, ChR2-eYFP virus was injected in PF and Cre-dependent mCherry virus was injected into STN of PV-Cre mice. To visualize $VGLUT2^+/PV^+$ neurons, Cre-dependent mCherry virus was injected into STN of Vglut2-Cre or PV-Cre mice. For HSV-based anterograde tracing, a Cre-dependent HSV system was injected into STN of PV-Cre mice, resulting in HSV-GFP labeling in downstream neurons. For CPu manipulation studies in PD mice, PD animals were generated by injecting retrograde RVdGL-Cre in CPu, Cre-dependent hM4Di-mCh ($PD_{hM4Di}$) or Cre-dependent mCh ($PD_{mCh}$) in PF, and 6-OHDA in SNc. $WT_{mCh}$ mice were generated by injecting retrograde RVdGL-Cre in CPu, Cre-dependent mCh in PF, and saline in SNc. During these CPu manipulations in PD mice, at baseline, mice received saline injections 40 min before the test. For *ex vivo* recordings from the PF→STN circuit in rescued PD mice, oChIEF-mCh virus was injected in PF and Cre-dependent GFP virus into STN of PD model mice using PV-Cre animals. For *ex vivo* recordings from *D1*/*D2* in NAc that receive PF input, oChIEF-mCh virus were injected into PF of D2-eGFP control and PD model mice. For *ex vivo* recordings that tested the effect of nAChR manipulations on the PF→CPu circuit in PD animals, oChIEF-mCh virus was injected in PF and 6-OHDA in SNc of wild type mice. For *ex vivo* recordings that tested the effect of nAChR manipulations on the PF→NAc circuit in PD animals, oChIEF-mCh virus was injected in PF and 6-OHDA in SNc of D2-eGFP mice. For AMPA/NMDA ratio recordings of the PF→STN circuit after rotarod in PD animals treated with a nAChR agonist, oChIEF-mCh virus was injected in PF and Cre-dependent GFP virus into STN of PD model mice using PV-Cre animals. For nAChR manipulations without/with the chemogenetic inhibition of $PV^+$ STN neurons during rotarod, Cre-dependent hM4Di virus was injected in STN and 6-OHDA in SNc of PV-Cre mice.

## Macaque surgery

All neurosurgical procedures were performed using sterile methods while the subject was anesthetized. For general anesthesia, monkeys were administered atropine (0.05 mg/kg, intramuscular) to decrease bronchial secretions before giving ketamine (15 mg/kg, intramuscular), and then propofol (6 mg/kg, i.v.) was given to maintain anesthesia. The anesthesia level was adjusted to eliminate movement as assessed by toe pinches. Corneal reflexes were consistently absent. The subject was placed on a standard operating table with constant heating and the head of the subject was rigidly fixed on a stereotaxic frame (KOPF, 1430). Electrocardiography, heart rate, oxygen saturation (SpO2) (range 95–100%), and rectal temperature (37.5–38.5°C) were continuously monitored by a physiological

monitor (Mindray, uMEC7). Coordinates for virus injection were guided by T1-weighted, magnetization prepared rapid gradient echo structural images (3T Tim Trio scanner, Siemens), and the standard monkey atlas. AAVretro-hSyn-mCherry was injected in nine sites covering the whole SNr, and a total volume of 27 μL virus was unilaterally injected in the SNr at the speed of 300 nL/min.

### Mouse model of Parkinson's disease

6-OHDA injections were performed using the same methods as those for virus injections. 400 nl of 6-OHDA (3 mg/ml, Sigma) dissolved in sterile saline (0.9%) containing ascorbic acid (0.2%) was injected in the following coordinates: (SNc) AP −3.08 mm, ML +/−1.2 mm, DV 4.5 mm. Control mice were injected with 400 nl of vehicle (i.e., saline with 0.02% ascorbic acid). A premedication of desipramine (25 mg/kg, Sigma) was administered to animals prior to injections of 6-OHDA, in order to increase the selectivity of 6-OHDA-induced lesions. Mice were supplemented with DietGel (Clear$H_2O$) for one-week post-surgery. All staining and behavioral experiments were performed at least 14 days following surgery, when the amount of dopamine depletion (based on immunostaining) was maximal and stable.

### Brain slice preparation

Mice (8–12 weeks old) were anesthetized with isoflurane, decapitated, and their brains were quickly removed. For AMPA/NMDA ratio recordings, coronal slices (300 μm thickness) were prepared in an oxygenated cutting solution at 4°C using a vibratome (Leica). The cutting solution contained (in mM): 30 NaCl, 4.5 KCl, 1.2 $NaH_2PO_4$, 194 sucrose, 26 $NaHCO_3$, 10 D-glucose, 0.2 $CaCl_2$, and 8 $MgSO_4$, saturated with 95% $O_2$ - 5% $CO_2$ (pH 7.3, osmolarity of 350 mOsm). Slices were recovered in ACSF at 33°C (+/− 0.5°C) for 15 min and then kept at room temperature for 1 hr before recordings. ACSF contained (in mM): 119 NaCl, 2.3 KCl, 2.5 $CaCl_2$, 1.3 $MgSO_4$, 26.2 $NaHCO_3$, 1 $NaH_2PO_4$, and 11 D-glucose, saturated with 95% $O_2$ - 5% $CO_2$ (pH 7.3, osmolarity of 300 mOsm). For all other recordings, brains were quickly removed and placed in ice-cold ACSF consisting of (in mM): 125 NaCl, 3 KCl, 1.25 $NaH_2PO_4$, 2 $MgSO_4$, 2 $CaCl_2$, 25 $NaHCO_3$, and 10 D-glucose. Slices were stored for 30 min at 33°C (+/− 0.5°C) and then kept at room temperature until recordings.

### *Ex vivo* electrophysiological recordings

Whole cell recordings in current clamp- or voltage clamp-mode were performed using an IR-DIC microscope (Olympus) with a water immersion 40X objective (NA 0.8), equipped with four automatic manipulators (Luigs and Neumann), a CCD camera (Hamamatsu Co), and Clampex 10.7 software. For all recordings, borosilicate glass pipettes were fabricated (Sutter Instrument) with resistances of 3.5 to 5 MΩ. The AMPA/NMDA ratio measurements were performed by adding 100 μM picrotoxin (Tocris) in the extracellular solution, and voltage clamp recordings were performed using the following intracellular solution (in mM): 120 cesium methansulfonate, 10 HEPES, 1.1 EGTA, 5 NaCl, 1.1 TEA-Cl, 4 Mg-ATP, 0.3 Na-GTP, 4 QX314, and 0.5% biocytin. The osmolarity of this intracellular solution was 298 mOsm and the pH was 7.2. AMPA/NMDA ratio is defined as the ratio of the EPSC peak at −70 mV to the EPSC magnitude at +40 mV (50 ms following stimulation). For

other recordings, pipettes were filled with the following intracellular solution (in mM): 110 K-gluconate, 40 KCl, 10 HEPES, 3 ATP, 0.5 GTP, 0.2 EGTA, and 0.5% biocytin. The osmolarity of this intracellular solution was 290 mOsm and the pH was 7.25. For light-induced synaptic current (eEPSCs) recordings, to avoid contamination with IPSCs, neurons were clamped at −70 mV, which is close to the chloride current reversal potential in our intracellular solution protocol. ACSF with the AMPA receptor blocker CNQX (10 μM, Tocris) or $GABA_A$ receptor blocker picrotoxin (100 μM) was perfused onto the GP or SNr-containing slices to pharmacologically examine the postsynaptic current receptor type. The monosynaptic nature of PF→CPu, PF→STN, and PF→NAc circuits were confirmed by sequential bath application of 1 μM TTX, 100 μM 4AP, and then 10 μM CNQX. A series of 500 ms suprathreshold currents were used to quantify the excitability with holding at −55 mV for PF neurons, and −70 mV for STN. Membrane time constant (tau) was measured with a single exponential fit of the voltage deflection produced by a small hyperpolarizing current injection from the holding potential (−70 mV). Input resistance ($R_{in}$) was calculated as the slope of linear fits of current-voltage plots generated from a series of increasing current injection steps. Shape parameters were measured from the first action potential with 200 ms current injection (from a holding potential of −70 mV). Recordings were amplified using up to two dual channel amplifiers (Molecular Devices), filtered at 2 kHz, digitized (20 kHz), and acquired through an ADC/DAC data acquisition unit (Instrutech) running on Igor Pro (Wavemetrics). Access resistance (RA) was monitored throughout the duration of the experiment, and data acquisition was suspended whenever RA was beyond 20 MΩ. Optogenetic stimulation was achieved through Polygon400 (Mightex) with built-in LED sources (470, 570, 600 nm). Light power on the sample was 20 $mW/mm^2$ except for recordings reported in Fig. 1d, which employed a range of intensities from 0–30 $mW/mm^2$ in 5 mW steps. Also, in Fig. 1d, all three PF circuits (i.e., PF→CPu, PF→STN, PF→NAc) were examined from each individual virus-expressing mouse. To test ChR2 expression, slices were stimulated with 5 Hz blue light pulses. To test eArch function, continuous yellow light was delivered to the slices. To test SOUL function, a 2 s blue light pulse was delivered for activation followed by a delay and then a 2 s orange light pulse was delivered for inactivation. To test synaptic connections, slices were stimulated with a single light pulse of 5 ms, repeated 10 times every 5 s, after which the average response was computed. Optical HFS protocol: baseline AMPA/NMDA ratio was acquired before the onset of the HFS protocol (100 blue light pulses of 2 ms each at a frequency of 100 Hz, repeated 5 times every 3 min) and the effect on synaptic strength was recorded. To test the effect of different molecular targets on synaptic plasticity in the PF→STN circuit of PD model mice, PNU282987[42] (1 μM, Catalog# P6499, Sigma), DAMGO[41] (30 μM, Catalog# E7384, Sigma), SNP[53] ($10^{-4}$ M, Catalog# 1614501, Sigma), and AG1478[54] (5 μM, Catalog# T4182, Sigma) were bath applied throughout the recordings. To test the effect of an $\alpha 6$ nAChR antagonist on PF→CPu circuit strength in PD model mice, evoked EPSCs of PF→CPu circuit was measured before and after bath application of α-Ctx MII[44] (100 nM, Catalog# 1340, Tocris). To test the effect of different molecular targets on the strength of PF inputs to $D1^+$ neurons in NAc in PD model mice, evoked EPSCs of PF→NAc circuit was measured before and after bath application of epibatidine[55] (1 μM, Catalog# E1145, Sigma), UB165[56] (1 μM, Catalog# 1348, Tocris), CC4[57] (10 μM, Catalog# 5236, Tocris), and PNU282987[42] (1 μM, Catalog# P6499, Sigma).

### *In vivo* genome editing

CRISPR-mediated *in vivo* genome editing experiments were performed as previously described[43]. Briefly, single guide RNA (sgRNA) candidates targeting *Chrna6*, *Chrna7*, and *Chrnb2* with high specificity and high efficiency were computationally identified from sgRNA libraries for genome-wide CRISPR knockout screening. Three U6-sgRNA(FE) gene fragments with the F+E tracrRNA backbone were synthesized by Integrated DNA Technologies (sequences are provided below, spacer sequences are capitalized). These fragments were cloned into the pX552-mCherry plasmid (*EGFP* in pX552 plasmid was replaced with *mCherry*, pX552 was obtained from Addgene, plasmid #60958) by Gibson assembly (NEB E2621X) to construct pX552–3xsgRNA(FE)-mCherry. These constructs were functionally validated in Neuro2A cells. The AAV vector was serotyped with $AAV_9$ coat proteins and packaged in house (~$8 \times 10^{12}$ genome copy (GC) $ml^{-1}$ viral titers). Each sgRNA AAV was combined with a Cre-dependent *SpCas9* AAV to restrict manipulations to $Cre^+$ neurons (i.e., using PV-Cre mice for *Chrna7* KD in STN $PV^+$ cells, D1-Cre mice for *Chrnb2* KD in NAc $D1^+$ cells, mice with AAVretro-Cre injections in CPu for *Chrna6* KD in $PF_{CPu}$ neurons). The AAV-DIO-SpCas9 plasmid was serotyped with $AAV_9$ coat proteins and packaged by the Viral Core at Boston Children's Hospital ($2 \times 10^{13}$ GC $ml^{-1}$ viral titer). For these *in vivo* genome editing experiments, a 1:1 mix of $AAV_9$-sgRNA-mCherry:$AAV_9$-DIO-SpCas9 was injected into the target brain regions. Target gene KD was validated by FISH staining.

**U6-sgChrna6-1(FE) sequence—**

agtggccaactccatcactaggggttcctgcggccgcacgcgtaaggtcgggcaggaagagggcctatttcccatgattccttcatat
ttgcatatacgatacaaggctgttagagagataattagaattaatttgactgtaaacacaaagatattagtacaaaatacgtgacgtagaa
agtaataatttcttgggtagtttgcagttttaaaattatgttttaaaatggactatcatatgcttaccgtaacttgaaagtatttcgatttcttggc
tttatatatcttgtggaaaggacgaaacaccgCAACCGCTTCATCCGGCCGGgtttaagagctatgctggaaacagc
atagcaagtttaaataaggctagtccgttatcaacttgaaaaagtggcaccgagtcggtgctttttttcccagtcacgacgttgtaaaacg
acggccagtgagcgcgcgtaatacgactcactatagg

**U6-sgChrna6-2(FE) sequence—**

cccagtcacgacgttgtaaaacgacggccagtgagcgcgcgtaatacgactcactataggaaggtcgggcaggaagagggcctat
ttcccatgattccttcatatttgcatatacgatacaaggctgttagagagataattagaattaatttgactgtaaacacaaagatattagtac
aaaatacgtgacgtagaaagtaataatttcttgggtagtttgcagttttaaaattatgttttaaaatggactatcatatgcttaccgtaacttg
aaagtatttcgatttcttggctttatatatcttgtggaaaggacgaaacaccgCTTTAAGAGCTCCTGCCCAAgtttaag
agctatgctggaaacagcatagcaagtttaaataaggctagtccgttatcaacttgaaaaagtggcaccgagtcggtgctttttttagcg
gataacaatttcacacaggaaacagctatgaccatgattacgccaagcgcgc

**U6-sgChrna6-3(FE) sequence—**

agcggataacaatttcacacaggaaacagctatgaccatgattacgccaagcgcgcaaggtcgggcaggaagagggcctatttccc
atgattccttcatatttgcatatacgatacaaggctgttagagagataattagaattaatttgactgtaaacacaaagatattagtacaaaat
acgtgacgtagaaagtaataatttcttgggtagtttgcagttttaaaattatgttttaaaatggactatcatatgcttaccgtaacttgaaagt
atttcgatttcttggctttatatatcttgtggaaaggacgaaacaccgAGGTTGATGGTGTAAAACATgtttaagagcta
tgctggaaacagcatagcaagtttaaataaggctagtccgttatcaacttgaaaaagtggcaccgagtcggtgctttttttctagactgc
agagggccctgcgtatgagtgcaagtgggttttaggaccaggatgaggcggggtg

**U6-sgChrna7-1(FE) sequence—**

agtggccaactccatcactaggggttcctgcggccgcacgcgtaaggtcgggcaggaagagggcctatttcccatgattccttcatat
ttgcatatacgatacaaggctgttagagagataattagaattaatttgactgtaaacacaaagatattagtacaaaatacgtgacgtagaa
agtaataatttcttgggtagtttgcagttttaaaattatgttttaaaatggactatcatatgcttaccgtaacttgaaagtatttcgatttcttggc
tttatatatcttgtggaaaggacgaaacaccgTTGGCCACCGGCCTCTCCAGgtttaagagctatgctggaaacagc
atagcaagtttaaataaggctagtccgttatcaacttgaaaaagtggcaccgagtcggtgctttttttcccagtcacgacgttgtaaaacg
acggccagtgagcgcgcgtaatacgactcactatagg

**U6-sgChrna7-2(FE) sequence—**

cccagtcacgacgttgtaaaacgacggccagtgagcgcgcgtaatacgactcactataggaaggtcgggcaggaagagggcctat
ttcccatgattccttcatatttgcatatacgatacaaggctgttagagagataattagaattaatttgactgtaaacacaaagatattagtac
aaaatacgtgacgtagaaagtaataatttcttgggtagtttgcagttttaaaattatgttttaaaatggactatcatatgcttaccgtaacttg
aaagtatttcgatttcttggctttatatatcttgtggaaaggacgaaacaccgCAAGACGTTGGTGTGGAATGgtttaa
gagctatgctggaaacagcatagcaagtttaaataaggctagtccgttatcaacttgaaaaagtggcaccgagtcggtgctttttttagc
ggataacaatttcacacaggaaacagctatgaccatgattacgccaagcgcgc

**U6-sgChrna7-3(FE) sequence—**

agcggataacaatttcacacaggaaacagctatgaccatgattacgccaagcgcgcaaggtcgggcaggaagagggcctatttccc
atgattccttcatatttgcatatacgatacaaggctgttagagagataattagaattaatttgactgtaaacacaaagatattagtacaaaat
acgtgacgtagaaagtaataatttcttgggtagtttgcagttttaaaattatgttttaaaatggactatcatatgcttaccgtaacttgaaagt
atttcgatttcttggctttatatatcttgtggaaaggacgaaacaccgGATCATCGTGGGCCTCTCAGgtttaagagcta
tgctggaaacagcatagcaagtttaaataaggctagtccgttatcaacttgaaaaagtggcaccgagtcggtgctttttttctagactgc
agagggccctgcgtatgagtgcaagtgggttttaggaccaggatgaggcggggtg

**U6-sgChrnb2-1(FE) sequence—**

agtggccaactccatcactaggggttcctgcggccgcacgcgtaaggtcgggcaggaagagggcctatttcccatgattccttcatat
ttgcatatacgatacaaggctgttagagagataattagaattaatttgactgtaaacacaaagatattagtacaaaatacgtgacgtagaa
agtaataatttcttgggtagtttgcagttttaaaattatgttttaaaatggactatcatatgcttaccgtaacttgaaagtatttcgatttcttggc
tttatatatcttgtggaaaggacgaaacaccgACGGATCAGCTTGTTATAGCgtttaagagctatgctggaaacagca
tagcaagtttaaataaggctagtccgttatcaacttgaaaaagtggcaccgagtcggtgctttttttcccagtcacgacgttgtaaaacga
cggccagtgagcgcgcgtaatacgactcactatagg

**U6-sgChrnb2-2(FE) sequence—**

cccagtcacgacgttgtaaaacgacggccagtgagcgcgcgtaatacgactcactataggaaggtcgggcaggaagagggcctat
ttcccatgattccttcatatttgcatatacgatacaaggctgttagagagataattagaattaatttgactgtaaacacaaagatattagtac
aaaatacgtgacgtagaaagtaataatttcttgggtagtttgcagttttaaaattatgttttaaaatggactatcatatgcttaccgtaacttg
aaagtatttcgatttcttggctttatatatcttgtggaaaggacgaaacaccgGCGAGGTGATGAGTACGCAGgtttaa
gagctatgctggaaacagcatagcaagtttaaataaggctagtccgttatcaacttgaaaaagtggcaccgagtcggtgctttttttagc
ggataacaatttcacacaggaaacagctatgaccatgattacgccaagcgcgc

**U6-sgChrnb2-3(FE) sequence—**

agcggataacaatttcacacaggaaacagctatgaccatgattacgccaagcgcgcaaggtcgggcaggaagagggcctatttccc
atgattccttcatatttgcatatacgatacaaggctgttagagagataattagaattaatttgactgtaaacacaaagatattagtacaaaat
acgtgacgtagaaagtaataatttcttgggtagtttgcagttttaaaattatgttttaaaatggactatcatatgcttaccgtaacttgaaagt
atttcgatttcttggctttatatatcttgtggaaaggacgaaacaccgTGTGCGTGGTAGGCGAACGGgtttaagagct

atgctggaaacagcatagcaagtttaaataaggctagtccgttatcaacttgaaaaagtggcaccgagtcggtgctttttttctagactg
cagagggccctgcgtatgagtgcaagtgggttttaggaccaggatgaggcggggtg

## Behavior assays

Experiments were conducted during the light cycle (7 am to 7 pm). Mice were randomly assigned to experimental groups for specific behaviors immediately after surgery. Mice were habituated to investigator handling for 1–2 minutes on three consecutive days. Handling took place in the holding room where the mice were housed. Prior to each handling session, mice were transported by wheeled cart to and from the vicinity of the behavior rooms to habituate them to the journey. All behavior experiments were analyzed blind to experimental group. Given behavioral variability, initial assays were performed using a minimum of 7–10 mice per group to ensure adequate power for any observed differences. Following behavioral protocols, brain sections were prepared to confirm efficient viral labeling in target areas. Animals lacking adequate labeling were excluded prior to behavior quantification. For oChIEF-mediated stimulation or eArch, NpHR-mediated inhibition experiments, optic fibers were connected to a 473 nm blue laser or a 570 nm yellow laser, respectively. For SOUL-mediated stimulation experiments, optic fibers were connected to a 473 nm blue laser for activation and a 600 nm orange laser for inactivation. Laser power was adjusted to 10–15 mW before each experiment. oChIEF-based optical LTP was induced with continuous 20 Hz blue light during trials combined with 100 Hz blue light (5 trains of 100 pulses, repeated 5 times every 3 min) between trials on the first day of training. For the forced swim and tail suspension tests, SOUL in PF thalamus was activated using a 60 s blue laser light source (activation) connected to the skull just before the start of the experiment, after this optic fibers were disconnected, and following the completion of the behavior mice were reconnected via optic fibers to a 90 s orange laser light source (inactivation). For sucrose preference tests, SOUL in PF thalamus was activated similar to the forced swim and tail suspension tests, except that mice remained plugged in to the optic fibers for the entire duration of the behavior and SOUL activation was performed for 5 minutes, followed by 5 minutes of inactivation, repeated for the session. For the $PD_{SOUL}$ control group, orange light was delivered *in vivo* immediately after blue light application. For optogenetic and chemogenetic inhibition experiments on the rotarod setup, yellow light or C21 were applied on the first training day. For hM4Di-mediated chemogenetic inhibition experiments, compound 21 (C21, Hello Bio) was injected intraperitoneally 40 min before each behavior test, at a dose of 2 mg $kg^{-1}$. For activation of $\alpha 7$ nAChRs in rotarod learning, PNU282987 was applied intraperitoneally (1.5 mg/kg) or locally infused into bilateral STN (1 μM, 250 nl per hemisphere) 40 min before training on the first day. For the inactivation of $\alpha 6$ nAChRs in open field tests, α-Ctx MII (100 nM, 1 μl per hemisphere, Tocris) was locally infused into bilateral CPu 40 mins before behavior. For the activation of $\beta 2$ nAChRs in depression-like behaviors, epibatidine (1 μM, 250 nl per hemisphere, Sigma) was locally infused into bilateral NAc 40 mins before behaviors.

**Open field test.—**Motor activity was measured in an open field arena (40 × 40 × 30 cm) for 20 min. Mice were transferred to the testing room and acclimated for 30 min before the test session. During the testing period, lighting in the room was turned off. The apparatus was cleaned with quatricide before and between runs. Movement of each animal

in the arena was detected using an automated infrared (IR) detection system (Omnitech Digiscan, AccuScan Instruments). Raw data were extracted using Microsoft Excel. For repeated open field tests with $PF_{CPu}$ manipulations, animals were habituated to the arena for three consecutive days (1 hr per day) before the first test. Z-scores for fraction of time spent moving, total distance traveled, and number of movements were calculated as $z = (x_i - \bar{x}) / (\sigma_x - n)$, where $x_i$ is the value for each animal, $\bar{x}$ is the mean value across all animals, $\sigma_x$ is the standard deviation across all animals. Z-score for each animal and each measure has been plotted with density clouds for each group overlaid. For distance traveled, number of movements, and moving time variables, we performed an ANOVA using group assignment (WT or PD) and time points (baseline, day 7, day 10) as predictors in a full linear model, including an interaction term between group assignment and time point. For all three variables individually, the ANOVA resulted in a significant interaction between group assignment and time point. Post-hoc two-sided *t* tests were performed between WT, $PD_{mCh}$, and $PD_{hM4Di}$ groups at each time point. *P* values were corrected for multiple comparisons using the Holm-Sidak method. For distance traveled, $WT_{mCh}$ vs. $PD_{hM4Di}$ group (Baseline: $P < 0.001$, day 7: NS, day 10: NS). For number of movements, $WT_{mCh}$ vs. $PD_{hM4Di}$ groups (Baseline: $P < 0.01$, day 7: NS, day 10: NS). For moving time, $WT_{mCh}$ vs. $PD_{hM4Di}$ groups (Baseline: $P < 0.01$, day 7: NS, day 10: NS). For distance traveled, $PD_{mCh}$ vs. $PD_{hM4Di}$ group (Baseline: NS, day 7: $P < 0.01$, day 10: $P < 0.05$). For number of movements, $PD_{mCh}$ vs. $PD_{hM4Di}$ groups (Baseline: NS, day 7: $P < 0.01$, day 10: $P < 0.01$). For moving time, $PD_{mCh}$ vs. $PD_{hM4Di}$ groups (Baseline: NS, day 7: $P < 0.05$, day 10: $P < 0.01$).

**Rotarod test.—**Mice were transferred to the testing room and acclimated for 15 min before the test session. Mice were placed on the rod (Med Associates) with the apparatus set to accelerating mode (4–40 r.p.m.). Latency to fall for each trial was automatically recorded by the apparatus. Each mouse was tested for three trials in a single day over two consecutive days, with a minimum of 15 min between trials. Raw data were recorded and analyzed using Microsoft Excel. Fall latency was averaged across three trials within each day, and then normalized to day 1 for each animal. For rotarod-induced STN *cFos* labeling or synaptic changes (measured using *ex vivo* electrophysiology), animals were sacrificed for IHC or slice recordings 1 hr after behavior training on day 1.

**Zero maze test.—**The elevated zero maze apparatus had four equally divided quadrants, specifically two open and two closed arms, and the setup was elevated ~2.5 ft above the floor. Using indirect lighting, the open arms were at 60 lux and the closed arms were at 10 lux. Mice were placed in the center of the closed arm and allowed to explore the arena for 5 min. Animal placement was counterbalanced. Anxiety-like behavior was assessed based on percentage of time spent in the open arms. Automated analysis was performed using the Noldus Observer software.

**Forced swim test.—**Mice were placed in cylindrical glass beakers (12 cm in diameter, 25 cm in height) filled with water at ~25°C, in which they could not touch the bottom of the beakers. Video recording was performed from the side view 2 min after mice were placed in the water, serving as a habituation period. Immobility time was measured for 4 min by

blind manual scoring. After testing, mice were placed in a pre-warmed cage for 30 min after which they were returned to their home cages.

**Tail suspension test.—**Mice were gently suspended using autoclaved tape to secure their tail to a horizontal bar 60 cm from the floor. We made sure that the animal could not make any contact or climb during testing. Video recording was performed 1 min after mice were inverted and taped, serving as a habituation period. Time spent struggling was measured for 5 min by blind manual scoring.

**Sucrose preference test.—**In the home cage, single housed mice were habituated to two identical bottles containing 1.5% sucrose solution for 2 days, followed by two identical water bottles for 1 day. Mice were water deprived for 1 day and then on the test day exposed to two bottles, one with water and the other containing 1.5% sucrose solution. The test duration was 4 hr in the dark, during which we switched the bottle locations at the 2 hr time point. Total consumption of water and sucrose solution was measured at the end of the session by weighing the bottles. Sucrose preference was defined as the ratio of the consumption of sucrose solution versus the consumption of both water and sucrose solution. Testing was performed over 3 consecutive days. For chemogenetic experiments, animals were injected with C21 30 min before testing.

**Contextual fear conditioning test.—**The conditioning context was a 29 × 25 × 22 cm chamber with grid floors, dim white lighting, and scented with 0.25% benzaldehyde. All mice were conditioned (120 s exploration, one 0.65 mA shock of 2 s duration at 120 s, 60 s post-shock period, second 0.65 mA shock of 2 s duration at 180 s, 60 s post-shock period), and tested (3 min) one day later. Floors of chambers were cleaned with quatricide before and between runs. Mice were transported to and from the experimental room in their home cages using a wheeled cart.

**Real-time place preference test.—**We placed mice in a custom-made behavioral arena (40 × 15 cm) for 10 min. We assigned one counterbalanced side of the chamber as the stimulation side (+light). We placed the mouse in the non-stimulation side (-light) at the onset of the experiment and each time the mouse crossed over to the stimulation side of the chamber, we delivered 20-Hz blue laser stimulation until the mouse crossed back into the non-stimulation side.

**Cocaine-induced conditioned place preference test.—**The conditioned place preference (CPP) behavior chamber was a rectangular arena (40 × 15 cm), divided into three quadrants (left, middle, right). The left and right quadrants were 15 cm long, while the middle quadrant was 13 cm long. The left quadrant had grid floors and a pattern (series of parallel lines) on the wall. The right quadrant had smooth polypropylene floors and a pattern (series of circles) on the wall. On day 1 (pre-exposure), mice were allowed to explore the entire arena for 30 min. Experiments showed no preference to any one quadrant. On day 2 (training), mice were confined to the left or right quadrants for 20 min following cocaine (20 mg $kg^{-1}$) or saline intraperitoneal administration. On days 3–7 (training continued), mice were conditioned in opposite quadrants in an alternating manner (i.e., cocaine left-saline right-cocaine left, etc.) until every mouse received 3 cocaine and 3

saline pairings. For every behavioral cohort, half the mice were conditioned with cocaine in the left quadrant, while the remaining mice received cocaine in the right quadrant. On day 8, memory recall was measured by preference to the left or right quadrant (10 min). All sessions were performed with dim white lighting. Mouse behavior, specifically position tracking and duration, was recorded using an automated infrared (IR) detection system (EthoVision XT, Noldus). The tracking software plotted heatmaps for each mouse, which was averaged to create representative heatmaps for each group. Raw data were extracted and analyzed using Microsoft Excel. For neuronal inhibition of $PF_{NAc}$, we injected C21 40 minutes before each training session.

## Fiber photometry

For *in vivo* imaging experiments, 250 nl of AAVretro-Cre virus was injected in CPu, STN, or NAc combined with a Cre-dependent GCaMP6s virus injected in PF (300 nl). After ~4 weeks of virus expression, an optic fiber (outer diameter of 200 μm, numerical aperture of 0.37, Inper) was implanted 200 μm above the PF injection site. Following another 1.5 weeks of recovery, imaging during behavioral paradigms was performed using the commercial Inper Fiber Photometry System (China). Behavior videos were collected using a driver-free camera, which was automatically driven by the InperStudio 3.1.1 software installed together with the Basler camera driver. Calcium signal acquisition and video recordings were synchronized with the same start/stop button in the InperStudio software. Each group experienced three different behaviors in the following order: open field (one 10 min session), rotarod (three trials on one day), and tail suspension (one 5 min session). 470 and 405 nm LEDs were used for GCaMP6s excitation and control signals, respectively. Power of the 470 nm LED was between 10–20 μW, and the 405 nm LED power was adjusted to approximately match the GCaMP fluorescence signal. Emitted signals were captured at 120 Hz with alternating pulses of 470 and 405 nm light resulting in frame rates of 60 Hz for GCaMP and control signals. Calcium activity data were analyzed using the InperDataProcess 3.1.1 software. To account for the effect of photobleaching caused by prolonged recording sessions, calcium signals were baseline corrected using the InperDataProcess software. Polynomial least squared regression was used to obtain the corrected calcium signals. Fitting the original data through the polynomial method generated a regression line, and signal correction was then conducted according to the predicted values from the regression line. In order to minimize motion-related artifacts, calcium signals were motion corrected using the InperDataProcess software. The 405 nm signal was scaled using least-squares regression and then subtracted from the 470 nm signal to generate the corrected 470 nm signal.

Event markers were manually labeled in the software using the synchronized behavioral videos. For the open field test, immobility start was defined by at least 2 s of complete immobility and immobility end was defined by at least 2 s of complete immobility followed by at least 2 second of movement. For the onset of immobility, we detected 75 epochs (10 + 13 + 20 + 13 + 19 from 5 mice) for the $PF_{CPu}$ group, 59 epochs (12 + 14 + 9 + 14 + 10 from 5 mice) for the $PF_{STN}$ group, and 68 epochs (14 + 14 + 13 + 13 + 14 from 5 mice) for the $PF_{NAc}$ group. For the end of immobility, we detected 71 epochs (10 + 12 + 19 + 12 + 18 from 5 mice) for the $PF_{CPu}$ group, 58 epochs (11 + 14 + 9 + 14 + 10 from 5 mice) for

the $PF_{STN}$ group, and 63 epochs (13 + 13 + 12 + 12 + 13 from 5 mice) for the $PF_{NAc}$ group. For the rotarod test, animals were placed on the rod rotating at a constant speed of 4 rpm during habituation. Acceleration start was defined as the initiation of the rotarod test. As the acceleration of the rod increased from 4 rpm, the time point at which animals dropped from the rod was defined as the end of acceleration. Each group experienced three trials on the same day. Thus, 15 epochs with 3 trials per animal were recorded for both onset and end of acceleration for each PF population. For the tail suspension test, struggling start was defined as at least 2 s of struggling followed by at least 2 s of complete immobility. Struggling end was defined as at least 2 s of immobility followed by at least 2 s of struggling. For the onset of struggling, we detected 45 epochs (9 + 12 + 9 + 7 + 8 from 5 mice) for the $PF_{CPu}$ group, 50 epochs (12 + 5 + 11 + 13 + 9 from 5 mice) for the $PF_{STN}$ group, and 52 epochs (14 + 9 + 13 + 9 + 7 from 5 mice) for the $PF_{NAc}$ group. For the end of struggling, we detected 45 epochs (9 + 12 + 9 + 7 + 8 from 5 mice) for the $PF_{CPu}$ group, 52 epochs (12 + 5 + 12 + 14 + 9 from 5 mice) for the $PF_{STN}$ group, and 52 epochs (13 + 8 + 14 + 10 + 7 from 5 mice) for the $PF_{NAc}$ group.

$\Delta F/F$ was calculated as the relative change of the GCaMP signal ($F_{(t)}$) during the designated epochs as compared to the mean value of the GCaMP signal during baseline ($F_0$): $\Delta F/F = \frac{F(t) - F0}{F0}$. For area under the curve (AUC) calculations, we used the following: For the open field test, baseline was set as a 4 s period prior to the onset of immobility (onset) and a 4 s period after the end of immobility (end); for the rotarod test, baseline was set as a 2 s period prior to the onset of acceleration (onset) and a 2 s period after the end of acceleration (end); for the tail suspension test, baseline was set as a 2 s period prior to the onset of struggling (onset) and a 2 s period after the end of struggling (end). AUC was calculated during the 4 s period after the onset or the 4 s period before the end of each epoch for open field, rotarod, and tail suspension tests. For the correlation plot of GCaMP intensity and mouse velocity in the open field test, baseline was calculated for each mouse using the averaged GCaMP signal during the immobile period (velocity = 0 cm/s detected with ANY-maze 6.35 software). For the correlation plot of GCaMP intensity and mouse velocity in the rotarod test, baseline was calculated for each mouse using the GCaMP signal 2 s prior to the onset of acceleration.

## Statistics and reproducibility

All experiments and data analyses were conducted blind to experimental groups. The number of replicates ($n$) is indicated in figure legends and refers to the number of experimental subjects independently treated in each experimental condition. Data are presented as mean values accompanied by SEM. Statistical comparisons were performed using Microsoft Excel with the Statplus plug-in, Python, and Prism 6 software. One-way ANOVA followed by Bonferroni post-hoc tests, two-way ANOVA with repeated measures followed by Bonferroni post-hoc tests, two-way ANOVA followed by post-hoc two-sided $t$ tests, unpaired $t$ test, and paired $t$ test were used to test for statistical significance when appropriate. No statistical methods were used to pre-determine sample sizes. Statistical significance threshold was set at $\alpha = 0.05$ (NS, $P > 0.05$; *, $P < 0.05$; **, $P < 0.01$; ***, $P < 0.001$). $P$ values are provided in all figure legends. Experiments were replicated in at least two independent batches that yielded consistent results.

## Extended Data

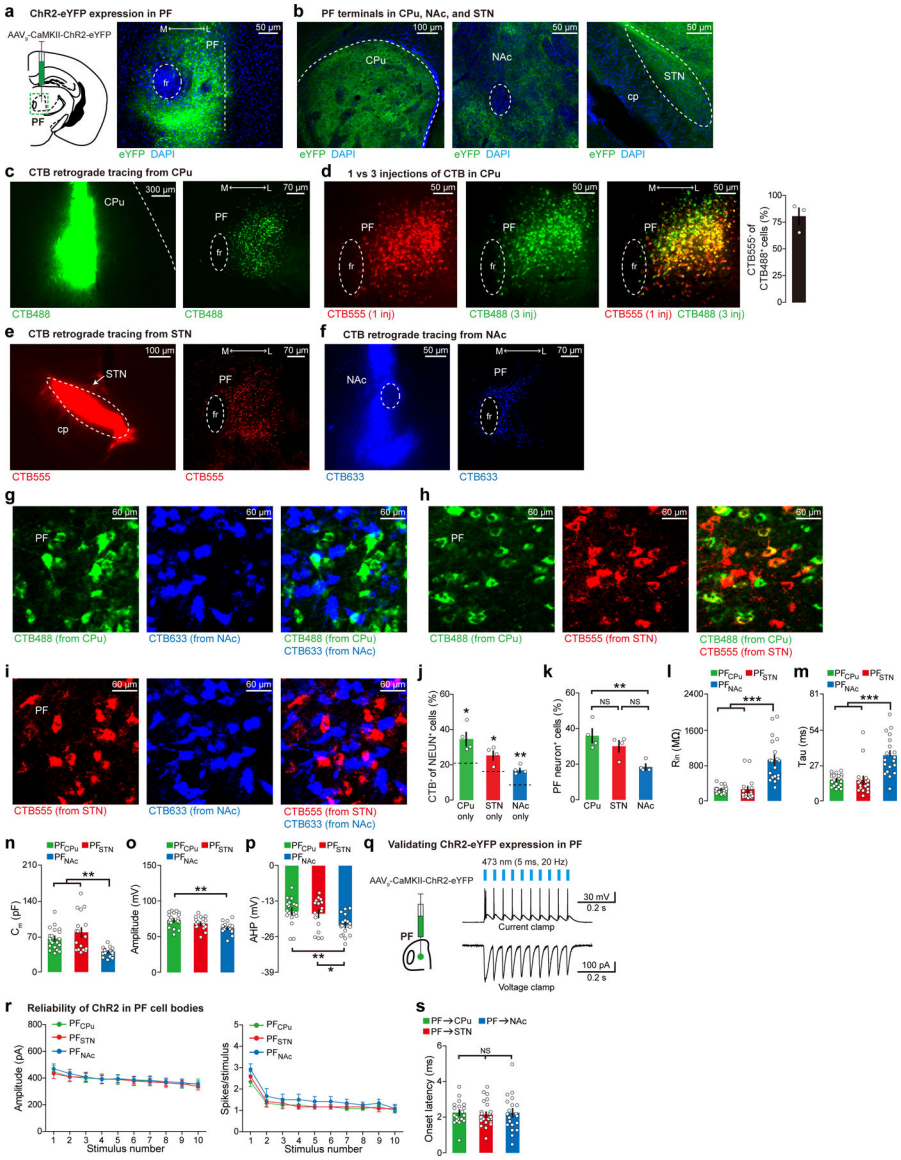


**Extended Data Fig. 1. PF projections to CPu, NAc, and STN, and $PF_{NAc}$ neurons have distinct electrophysiological properties as compared to $PF_{CPu}$ and $PF_{STN}$ populations.**

**a**-**b**, Anterograde tracing from mouse PF, ChR2-eYFP virus injection site (**a**), and PF terminals in CPu, NAc, and STN (**b**). DAPI staining (blue). **c**, CTB488 injection site in CPu (left) along with corresponding upstream PF labeling (lower magnification image relative to Fig. 1a, right). **d**, Upstream labeling in PF with 1 (CTB555) vs. 3 (CTB488) injections in CPu. 80.5% of CPu-projecting PF neurons (i.e., CTB488) are labeled by a single injection of CTB555 in CPu ($n$ = 3 mice). **e**-**f**, Injection sites of CTB555 in STN (left) (**e**) and CTB633 in NAc (left) (**f**) along with corresponding upstream PF labeling images (lower magnification relative to Fig. 1a, both right panels). **g**-**i**, Representative high magnification images from Fig. 1a, showing low overlap between CPu- and NAc-projecting PF neurons (**g**), CPu- and STN-projecting PF neurons (**h**), and STN- and NAc-projecting PF neurons

(**i**). **j**, Percentage of $CTB488^+$ only (CPu only), $CTB555^+$ only (STN only), and $CTB633^+$ only (NAc only) in PF. Dashed lines indicate chance level (20.49% for CPu only, 15.7% for STN only, 8.28% for NAc only) calculated using *NEUN* staining ($n = 4$ mice per group). **k**, Percentage of $NEUN^+$ PF neurons projecting to the three different targets ($n = 4$ mice per group). **l-p**, Electrophysiological properties of $PF_{CPu}$, $PF_{NAc}$, and $PF_{STN}$ neurons, which were labeled using retrograde RV injected into CPu, NAc, and STN respectively. Input resistance ($R_{in}$) (**l**), membrane time constant (tau) (**m**), membrane capacitance ($C_m$) (**n**), action potential amplitude (**o**), and action potential afterhyperpolarization (AHP) amplitude (**p**) (For $R_{in}$, tau, and $C_m$, $PF_{CPu}$: $n = 20$ neurons (7, 7, 6), $PF_{STN}$: $n = 17$ neurons (6, 5, 6), $PF_{NAc}$: $n = 19$ neurons (6, 7, 6) from 3 mice each. For amplitude and AHP, $PF_{CPu}$: $n = 18$ neurons (5, 5, 8), $PF_{STN}$: $n = 16$ neurons (6, 5, 5), $PF_{NAc}$: $n = 19$ neurons (6, 7, 6) from 3 mice each). **q**, ChR2-eYFP virus was injected in PF and *ex vivo* recordings were performed at PF cell bodies to validate virus expression (left), light responses in ChR2-labeled PF neurons were evoked by a 473 nm pulse train, shown in both current and voltage clamp modes (right). **r**, Reliability of ChR2 was compared across PF populations by recording from retrogradely-labeled $CTB^+$ neurons that also expressed ChR2 ($n = 12$ neurons (4, 4, 4) from 3 mice for each group). **s**, Onset latency of evoked EPSCs recorded in postsynaptic neurons receiving PF input (PF→CPu: $n = 19$ neurons (7, 6, 6), PF→STN: $n = 26$ neurons (10, 9, 7), PF→NAc: $n = 20$ neurons (7, 7, 6) from 3 mice each). Data are presented as mean ± SEM; $*P < 0.05$, $**P < 0.01$, $***P < 0.001$. NS, not significant. One-sample *t* test (**j**), one-way ANOVA followed by Bonferroni post-hoc test (**k**-**p**, **s**), and two-way ANOVA with repeated measures followed by Bonferroni post-hoc test (**r**). CPu only $P = 0.033$, STN only $P = 0.028$, NAc only $P = 0.006$ (**j**), $F = 8.88$, $P = 0.007$, CPu vs. STN $t = 1.4$, STN vs. NAc $t = 2.74$, CPu vs. NAc $t = 4.14$ (**k**), $F = 27.71$, $P < 0.0001$, $PF_{CPu}$ vs. $PF_{NAc}$ $t = 6.57$, $PF_{STN}$ vs. $PF_{NAc}$ $t = 6.28$ (l), $F = 17.48$, $P < 0.0001$, $PF_{CPu}$ vs. $PF_{NAc}$ $t = 5.17$, $PF_{STN}$ vs. $PF_{NAc}$ $t = 5.04$ (**m**), $F = 11.76$, $P < 0.0001$, $PF_{CPu}$ vs. $PF_{NAc}$ $t = 3.37$, $PF_{STN}$ vs. $PF_{NAc}$ $t = 4.69$ (**n**), $F = 7.19$, $P = 0.0018$, $PF_{CPu}$ vs. $PF_{NAc}$ $t = 3.78$ (**o**), $F = 6.11$, $P = 0.0042$, $PF_{CPu}$ vs. $PF_{NAc}$ $t = 3.26$, $PF_{STN}$ vs. $PF_{NAc}$ $t = 2.65$ (**p**), Amplitude: $F = 0.03$, DFn = 2, DFd = 297, $P = 0.97$, spikes/stimulus: $F = 0.68$, DFn = 2, DFd = 297, $P = 0.51$ (**r**), $F = 0.11$, $P = 0.89$ (**s**).

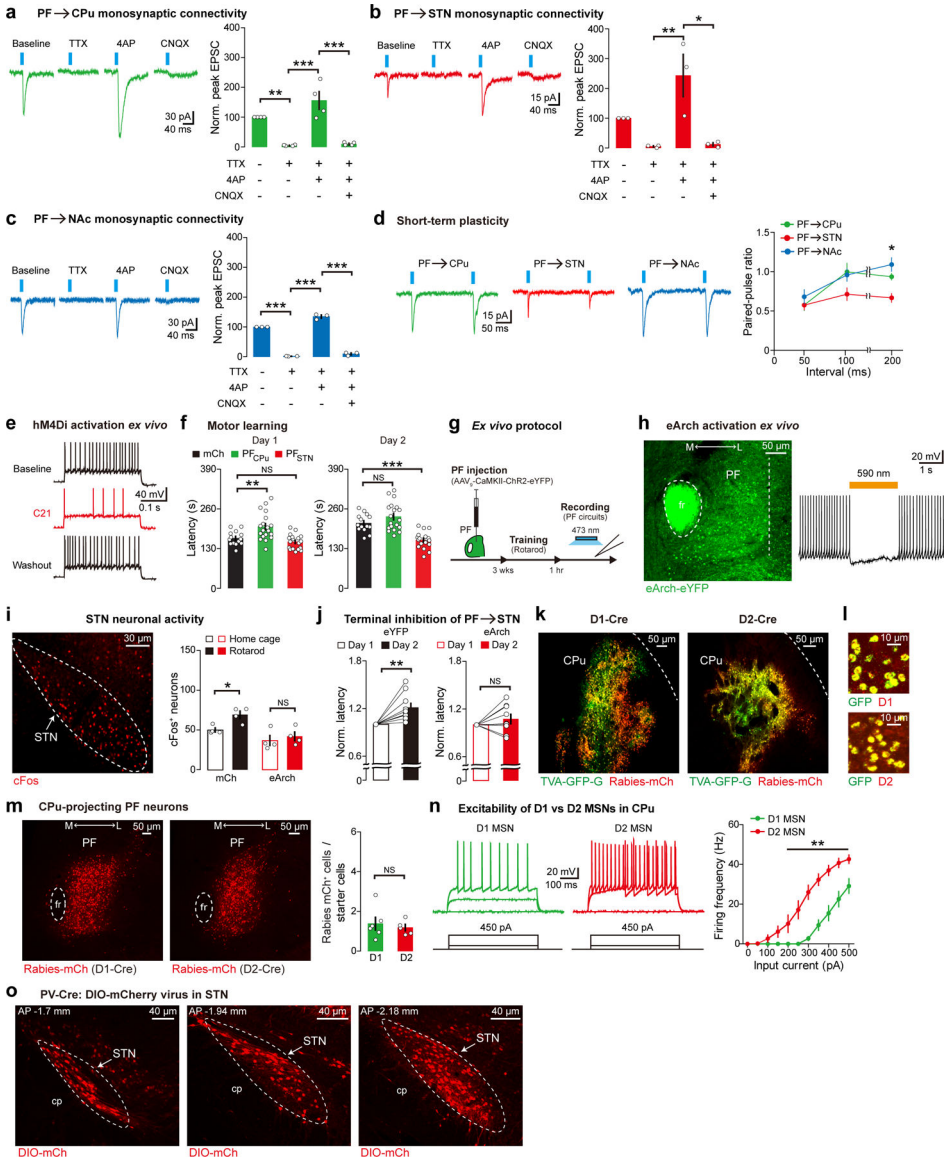


**Extended Data Fig. 2. PF circuit electrophysiology, PF→STN terminal inhibition during motor learning, and cell type-specific tracing for the PF→CPu circuit.**

**a-c**, Representative traces and quantification of evoked EPSCs in the presence of tetrodotoxin (TTX), 4-aminopyridine (4AP), and 6-cyano-7-nitroquinovaline-2,3-dione (CNQX) for PF→CPu (**a**), PF→STN (**b**), and PF→NAc (**c**) circuits (PF→CPu: $n = 4$ neurons (2, 1, 1), PF→STN: $n = 3$ neurons (1, 1, 1), PF→NAc: $n = 3$ neurons (1, 1, 1) from 3 mice each). Norm. peak EPSC amplitude plotted. **d**, Representative traces and quantification of paired-pulse ratio (also referred to as short-term plasticity) recordings in PF circuits (PF→CPu: $n = 20$ neurons (7, 6, 7), PF→STN: $n = 23$ neurons (8, 7, 8), PF→NAc: $n = 20$ neurons (7, 6, 7) from 3 mice each). **e**, C21-induced, reversible neuronal inhibition of a PF neuron expressing hM4Di *ex vivo*, using a step current injection protocol. **f**, C21-induced inhibition of $PF_{CPu}$ or $PF_{STN}$ neurons during rotarod tests ($n = 14$ mCh, $n = 19$ $PF_{CPu}$, $n = 18$ $PF_{STN}$ mice). **g**, Experimental protocol for AMPA/NMDA ratio recordings. CaMKII-ChR2-eYFP virus was injected in PF, 3 weeks later animals were trained on the

rotarod paradigm, and 1 hr after the end of training *ex vivo* recordings were performed. **h**, CaMKII-eArch3.0-eYFP virus was injected in PF and fibers were implanted above STN. eArch-eYFP virus expression in PF (left), and light-induced neuronal inhibition *ex vivo* (right). **i**, PF→STN terminal inhibition followed by *cFos* staining in STN using home cage or rotarod mice validated effective *in vivo* terminal inhibition ($n = 4$ mice per group). cFos was stained using a 633 secondary antibody (pseudocolored red). **j**, PF→STN terminal inhibition during rotarod. *eYFP* control mice received a CaMKII-eYFP virus in PF in place of the *eArch* virus. Norm. latency plotted relative to day 1 ($n = 10$ eYFP, $n = 9$ eArch mice). **k-m**, Monosynaptic retrograde RV tracing from $D1^+$ or $D2^+$ MSNs in CPu. Images show starter cells (**k**), FISH co-staining of *GFP* with *D1* or *D2* (**l**), and corresponding PF labeling (**m**) ($n = 6$ D1-Cre, $n = 5$ D2-Cre mice). **n**, Representative traces (left) and current-frequency curves (right) of *ex vivo* recordings from $D2^-$ (putative $D1^+$) or $D2^+$ MSNs in CPu (*D1*: $n =$ 14 neurons (5, 4, 5), *D2*: $n = 12$ neurons (4, 5, 3) from 3 mice each). **o**, Anterior to posterior (AP) distribution of *PV* neurons in STN. Cre-dependent mCh virus was injected into STN of PV-Cre mice. Data are presented as mean ± SEM; $*P < 0.05$, $**P < 0.01$, $***P < 0.001$. NS, not significant. One-way ANOVA followed by Bonferroni post-hoc test (**a-c**, **f**), two-way ANOVA with repeated measures followed by Bonferroni post-hoc test (**d**, **n**), unpaired *t* test (**i**, **m**), and two-tailed paired *t* test (**j**). $F = 24.64$, $P < 0.0001$, Baseline vs. TTX $t = 4.56$, TTX vs. TTX + 4AP $t = 7.23$, TTX + 4AP vs. TTX + 4AP + CNQX $t = 6.99$ (**a**), $F = 9.59$, $P = 0.005$, TTX vs. TTX + 4AP $t = 4.71$, TTX + 4AP vs. TTX + 4AP + CNQX $t = 4.57$ (**b**), $F = 468.7$, $P < 0.0001$, Baseline vs. TTX $t = 22.74$, TTX vs. TTX + 4AP $t = 30.83$, TTX + 4AP vs. TTX + 4AP + CNQX $t = 28.97$ (**c**), $F = 6.41$, DFn = 2, DFd = 120, $P = 0.003$ (**d**), Day 1: $F = 11.30$, $P < 0.0001$, mCh vs. $PF_{CPu}$ $t = 3.25$, mCh vs. $PF_{STN}$ $t = 1.00$, Day 2: $F = 22.58$, $P < 0.0001$, mCh vs. $PF_{CPu}$ $t = 1.70$, mCh vs. $PF_{STN}$ $t = 4.38$ (**f**), mCh $P = 0.012$, eArch $P = 0.55$ (**i**), eYFP $P = 0.0032$, eArch $P = 0.24$ (**j**), $P = 0.61$ (**m**), $F = 28.31$, DFn = 1, DFd = 240, $P < 0.0001$ (**n**).

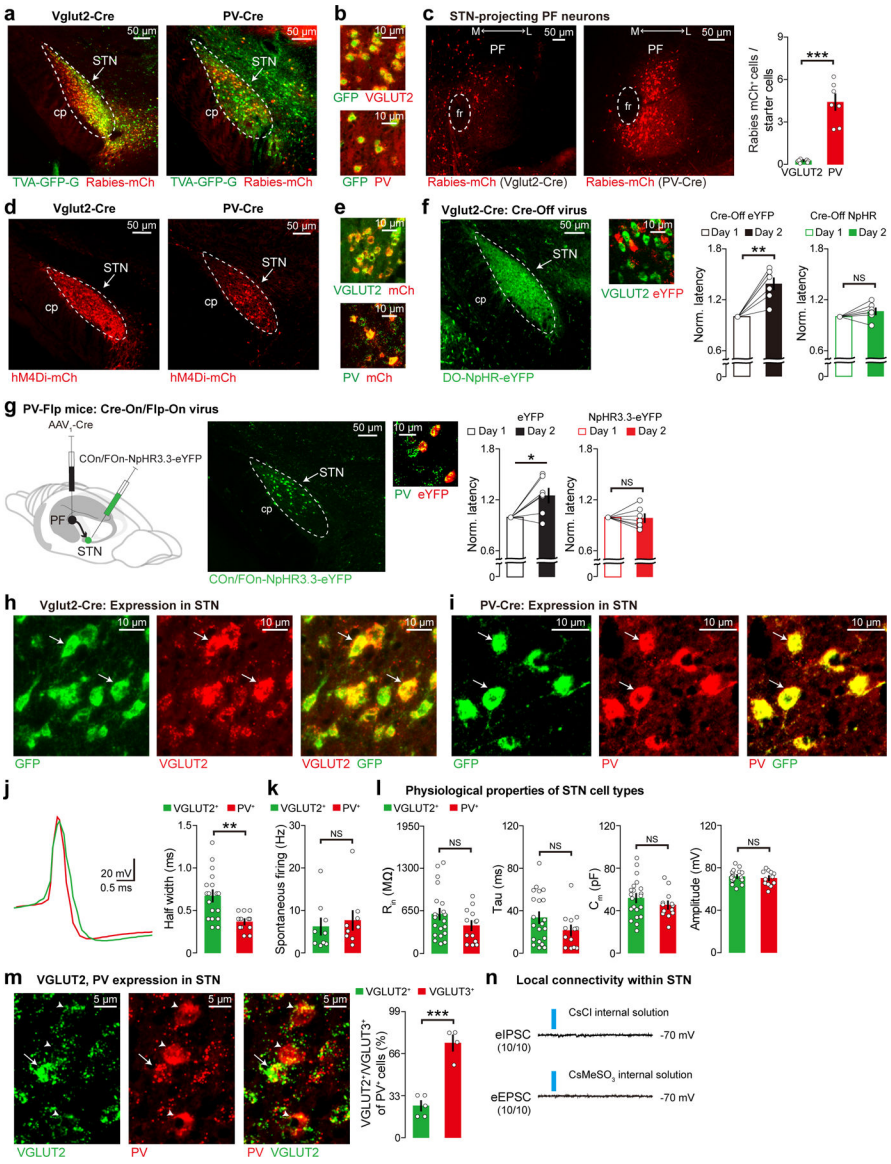


**Extended Data Fig. 3. Cell type-specific tracing for the PF→STN circuit, and *PV*$^+$ STN neurons are critical for motor learning, are excitatory in nature, and lack local STN connectivity.**

**a-c**, Monosynaptic retrograde RV tracing from *VGLUT2*$^+$ or *PV*$^+$ STN neurons. Images show starter cells in STN (**a**), FISH co-staining of *GFP* with *VGLUT2* or *PV* (**b**), and corresponding PF labeling (**c**, lower magnification image relative to Fig. 2h) ($n$ = 7 mice per group). **d-e**, Expression of a Cre-dependent hM4Di-mCh virus in STN (**d**), FISH co-staining of *mCh* with *VGLUT2* or *PV* (**e**) in Vglut2-Cre or PV-Cre mice, related to experiments in Fig. 2j–k. **f**, Inhibition of STN *VGLUT2*$^-$ neurons during rotarod using a Cre-Off virus (DO-NpHR-eYFP) injected in STN of Vglut2-Cre mice. *eYFP* mice received a control Cre-Off virus (DO-eYFP) in place of the NpHR virus ($n$ = 7 mice per group). FISH co-staining of *VGLUT2* with *eYFP* (used a red fluorophore to visualize the *eYFP* probe). **g**, Inhibition of STN *PV*$^+$ neurons that receive PF inputs during rotarod using an anterograde AAV expressing Cre injected in PF, and a Cre-On/Flp-On virus (COn/FOn-NpHR3.3-eYFP) injected in STN of PV-Flp mice. *eYFP* mice received a control Cre-On/Flp-On virus (COn/

FOn-eYFP) in place of the NpHR3.3 virus ($n$ = 7 mice per group). FISH co-staining of *PV* with *eYFP* (used a red fluorophore to visualize the *eYFP* probe). **h-i**, FISH staining of GFP-labeled *VGLUT2*$^+$ neurons and endogenous *VGLUT2* expression (**h**) or GFP-labeled *PV*$^+$ neurons and endogenous *PV* expression (**i**) showed a high degree of overlap for each of these mouse lines. *GFP* labeling was achieved by injecting a Cre-dependent AAV in STN of Vglut2-Cre or PV-Cre mice. **j-k**, Half width (**j**) and spontaneous firing (**k**) measured in *ex vivo* recordings from STN *VGLUT2*$^+$ and *PV*$^+$ neurons. To visualize *VGLUT2*$^+$ and *PV*$^+$ neurons, a Cre-dependent *mCh* virus was injected in STN of Vglut2-Cre or PV-Cre mice (Half width, *VGLUT2*$^+$: $n$ = 18 neurons (6, 5, 7), *PV*$^+$: $n$ = 12 neurons (4, 4, 4) from 3 mice each; Spontaneous firing, *VGLUT2*$^+$: $n$ = 9 neurons (3, 3, 3), *PV*$^+$: $n$ = 9 neurons (3, 3, 3) from 3 mice each). **l**, Input resistance ($R_{in}$), membrane time constant (tau), membrane capacitance ($C_m$), and action potential amplitude of STN *VGLUT2*$^+$ and *PV*$^+$ neurons. To visualize *VGLUT2*$^+$ and *PV*$^+$ neurons, a Cre-dependent *mCh* virus was injected in STN of Vglut2-Cre or PV-Cre mice ($R_{in}$, tau, and $C_m$, *VGLUT2*$^+$: $n$ = 21 neurons (8, 8, 5), *PV*$^+$: $n$ = 13 neurons (5, 5, 3) from 3 mice each; Amplitude, *VGLUT2*$^+$: $n$ = 18 neurons (6, 5, 7), *PV*$^+$: $n$ = 12 neurons (4, 4, 4) from 3 mice each). **m**, *VGLUT2*, *PV* FISH staining in wild type STN sections. Plot (right) shows the proportion of *VGLUT2*$^+$ or *VGLUT3*$^+$ neurons among the total number of *PV*$^+$ STN neurons ($n$ = 5 *VGLUT2*$^+$, $n$ = 4 *VGLUT3*$^+$ mice). **n**, Representative traces of evoked IPSCs ($n$ = 10 neurons (3, 4, 3) from 3 mice) and evoked EPSCs ($n$ = 10 neurons (2, 4, 4) from 3 mice) recorded in STN neurons during activation of ChR2-eYFP-expressing *PV*$^+$ STN neurons. PV-Cre mice were injected with a Cre-dependent ChR2-eYFP virus in STN. Data are presented as mean ± SEM; *$P$ < 0.05, **$P$ < 0.01, ***$P$ < 0.001. NS, not significant. Two-tailed unpaired $t$ test (**c**, **j-m**) and two-tailed paired $t$ test (**f**, **g**). $P$ < 0.0001 (c), Cre-Off eYFP $P$ = 0.001, Cre-Off NpHR $P$ = 0.12 (**f**), eYFP $P$ = 0.019, NpHR3.3 $P$ = 0.85 (**g**), $P$ = 0.0012 (**j**), $P$ = 0.62 (k), $R_{in}$ $P$ = 0.14, Tau $P$ = 0.11, $C_m$ $P$ = 0.26, Amplitude $P$ = 0.51 (**l**), $P$ = 0.0001 (**m**).

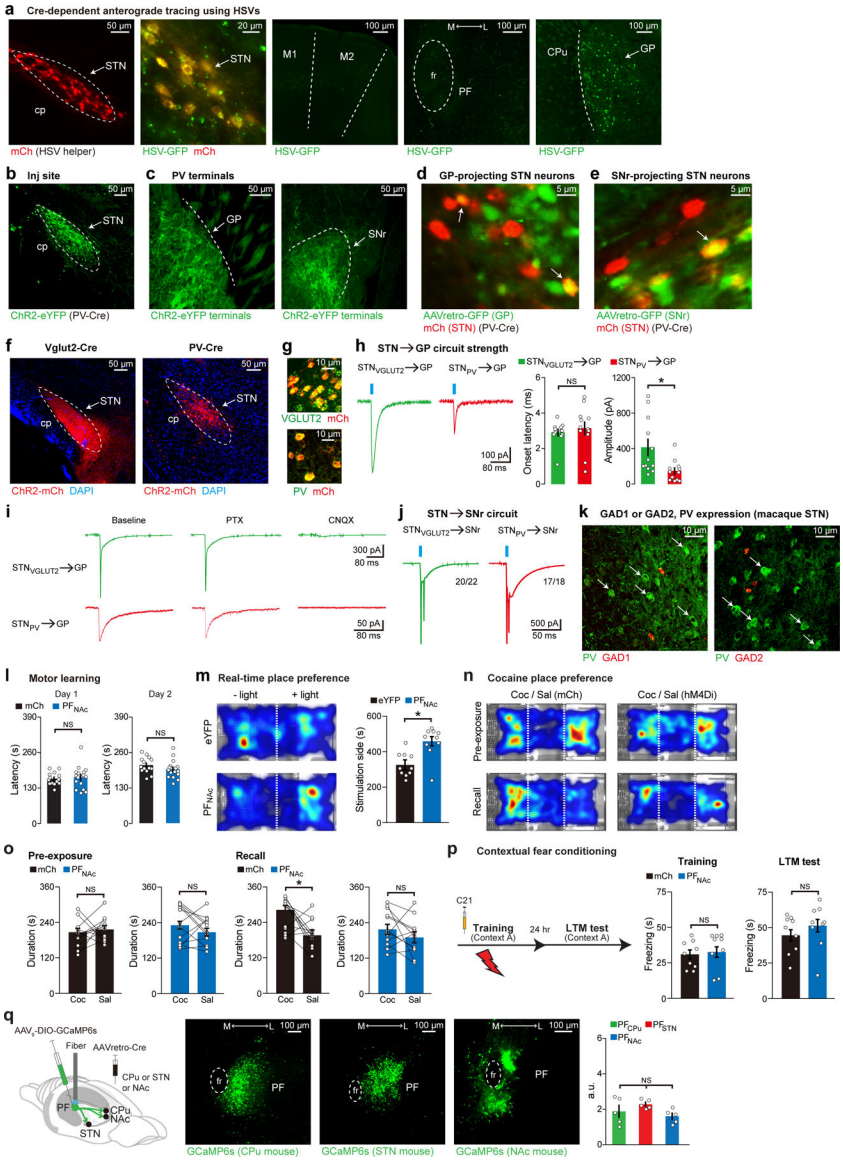


**Extended Data Fig. 4. *PV*$^+$ STN neurons send excitatory projections to GP and SNr, and PF$_{NAc}$ manipulations in motor, positive valence, and negative valence behaviors.**

**a**, Monosynaptic HSV anterograde tracing from *PV*$^+$ neurons in STN, using PV-Cre mice. Images show HSV helper cells (red) in STN overlapping with HSV-GFP-expressing cells (green) (i.e., starter cells), lack of labeling in known input brain regions (motor cortex, M1/M2 or PF thalamus) indicating that this virus does not travel retrogradely, and anterograde labeling in GP. **b-c**, Cre-dependent ChR2-eYFP virus injection (inj) site of PV-Cre mice (**b**), and representative images showing eYFP$^+$ axonal terminals in GP and SNr (**c**). **d-e**, Retrogradely-labeled neurons (green) from GP (**d**) or SNr (**e**) colocalized with *PV*$^+$ neurons in STN. Retrograde labeling was achieved by injecting AAVretro-GFP in GP or SNr. *PV* neurons were labeled by injecting a Cre-dependent *mCh* virus in STN of PV-Cre mice. **f-g**, Expression of Cre-dependent ChR2-mCh virus in STN of Vglut2-Cre or PV-Cre mice (**f**), FISH co-staining of *mCh* with *VGLUT2* or *PV* (**g**). DAPI staining (blue). **h**, Representative traces, onset latency, and amplitude of evoked EPSCs recorded in GP

neurons during terminal activation of STN *VGLUT2*$^+$ or *PV*$^+$ neurons ($STN_{VGLUT2}$→GP: $n$ = 12 neurons (4, 5, 3), $STN_{PV}$→GP: $n$ = 12 neurons (4, 4, 4) from 3 mice each). i, Representative traces of evoked EPSCs in the presence of picrotoxin (PTX) and 6-cyano-7-nitroquinovaline-2,3-dione (CNQX) for the $STN_{VGLUT2}$→GP and $STN_{PV}$→GP circuits. **j**, Representative traces of evoked EPSCs recorded in SNr neurons during activation of STN *VGLUT2*$^+$ or *PV*$^+$ neuronal terminals ($STN_{VGLUT2}$→SNr: $n$ = 22 neurons (6, 8, 8), $STN_{PV}$→SNr: $n$ = 18 neurons (6, 6, 6) from 3 mice each). **k**, *GAD1* or *GAD2* FISH with *PV* immunostaining in STN sections of cynomolgus macaques. **l**, C21-induced inhibition of $PF_{NAc}$ neurons during rotarod tests. *mCh* control mice data from Extended Data Fig. 2f ($n$ = 14 mCh, $n$ = 16 $PF_{NAc}$ mice). **m**, Real-time place preference behavior. NAc-projecting PF neurons were labeled by injecting RVdGL-Cre in NAc and Cre-dependent ChR2-eYFP in PF. Control group received the same injections except with Cre-dependent *eYFP* in PF. Blue light activation was performed at 20 Hz, only in the right side of the chamber (10 mW at patch cord) ($n$ = 10 mice per group). **n-o**, Cocaine-induced conditioned place preference behavior, heat maps (**n**), quantification (**o**). NAc-projecting PF neurons were labeled by injecting RVdGL-Cre in NAc and Cre-dependent hM4Di-mCh in PF (referred to as hM4Di or $PF_{NAc}$ groups). Control group received the same injections except with Cre-dependent *mCh* in PF (mCh group). Baseline preference in the 3-chamber arena referred to as pre-exposure. After cocaine-induced training was completed (left side for cocaine, right side for saline), recall tests demonstrated conditioned place preference. C21-induced inhibition of $PF_{NAc}$ neurons was performed during the training phase ($n$ = 12 mice per group). **p**, Contextual fear conditioning behavior. Mice were prepared similar to panel **n**. C21-induced inhibition was performed by injecting C21 40 min before the training day, followed by a long-term memory (LTM) test 24 hr later ($n$ = 9 mice per group). **q**, Fiber photometry recordings from $PF_{CPu}$, $PF_{STN}$, or $PF_{NAc}$ neurons by injecting a retrograde AAV expressing Cre in CPu, STN, or NAc, and Cre-dependent GCaMP6s in PF, followed by fibers placed above PF (left). Representative images (middle). Baseline *in vivo* GCaMP expression level (arbitrary units or a.u.) (right). Data are presented as mean ± SEM; *$P$ < 0.05. NS, not significant. Two-tailed unpaired $t$ test (**h**, **l** , **m**, **p**), two-tailed paired $t$ test (**d**), and one-way ANOVA followed by Bonferroni post-hoc test (**q**). Onset latency $P$ = 0.56, amplitude $P$ = 0.012 (**h**), Day 1 $P$ = 0.69, Day 2 $P$ = 0.20 (**l**), $P$ = 0.01 (**m**), Pre-exposure: mCh $P$ = 0.46, $PF_{NAc}$ $P$ = 0.34, Recall: mCh $P$ = 0.02, $PF_{NAc}$ $P$ = 0.21 (**o**), Training $P$ = 0.89, LTM test $P$ = 0.38 (**p**), $F$ = 2.17, $P$ = 0.16 (**q**).

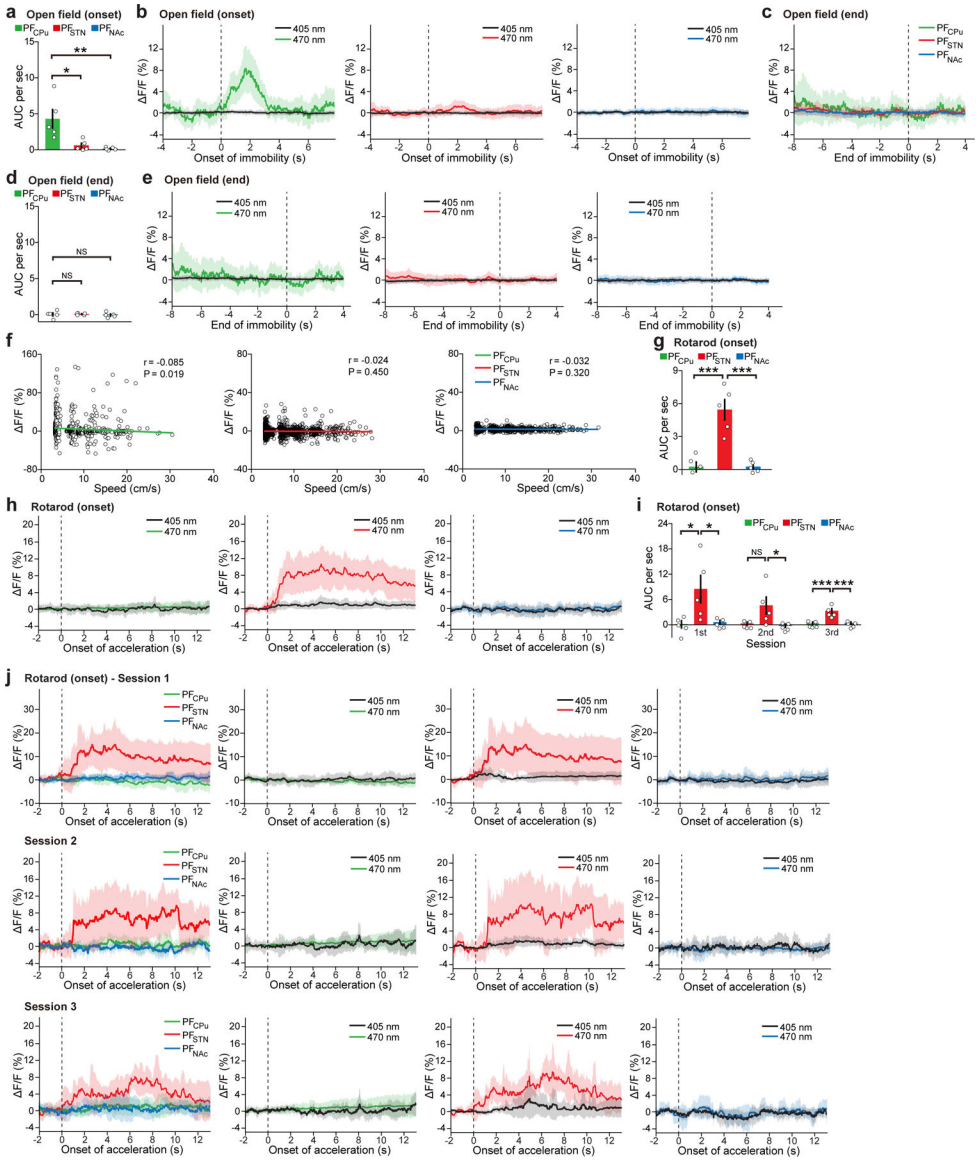


**Extended Data Fig. 5. *In vivo* fiber photometry analyses for open field and rotarod recordings.** **a-f**, Area under the curve (AUC) per sec for open field aligned to the onset of immobility (0 to 4 s compared to baseline −4 to 0 s) (**a**), 405 and 470 nm traces for each PF population for open field recordings aligned to the onset of immobility (**b**), averaged fluorescence change aligned to the end of immobility (**c**), AUC per sec for open field aligned to the end of immobility (−4 to 0 s compared to baseline 0 to 4 s) (**d**), 405 and 470 nm traces for each PF population for open field recordings aligned to the end of immobility (**e**), correlation between fluorescence change and mouse speed in the open field (r, correlation coefficient) (*n* = 5 mice per group) (**f**). **g-j**, AUC per sec for rotarod aligned to the onset of acceleration (0 to 4 s compared to baseline −2 to 0 s) (**g**), 405 and 470 nm traces for each PF population for rotarod recordings aligned to the onset of acceleration (**h**), AUC per sec for rotarod aligned to the onset of acceleration (0 to 4 s compared to baseline −2 to 0 s) for each individual session (**i**), 405 and 470 nm traces for each PF population for rotarod recordings aligned to

the onset of acceleration showing individual session data ($n$ = 5 mice per group) (**j**). Data are presented as mean ± SEM; *$P$ < 0.05, **$P$ < 0.01, ***$P$ < 0.001. NS, not significant. One-way ANOVA followed by Bonferroni post-hoc test (**a**, **d**, **g**, **i**) and correlation analysis (**f**). $F$ = 8.83, $P$ = 0.004, $PF_{CPu}$ vs. $PF_{STN}$ $t$ = 3.42, $PF_{CPu}$ vs. $PF_{NAc}$ $t$ = 3.83 (**a**), $F$ = 0.168, $P$ = 0.84, $PF_{CPu}$ vs. $PF_{STN}$ $t$ = 0.19, $PF_{CPu}$ vs. $PF_{NAc}$ $t$ = 0.38 (**d**), $F$ = 24.49, $P$ < 0.0001, $PF_{CPu}$ vs. $PF_{STN}$ $t$ = 6.07, $PF_{STN}$ vs. $PF_{NAc}$ $t$ = 6.05 (**g**), 1st: $F$ = 5.75, $P$ = 0.02, $PF_{CPu}$ vs. $PF_{STN}$ $t$ = 3.02, $PF_{STN}$ vs. $PF_{NAc}$ $t$ = 2.85, 2nd: $F$ = 4.816, $P$ = 0.03, $PF_{CPu}$ vs. $PF_{STN}$ $t$ = 2.54, $PF_{STN}$ vs. $PF_{NAc}$ $t$ = 2.82, 3rd: $F$ = 17.28, $P$ = 0.0003, $PF_{CPu}$ vs. $PF_{STN}$ $t$ = 5.13, $PF_{STN}$ vs. $PF_{NAc}$ $t$ = 5.05 (**i**).

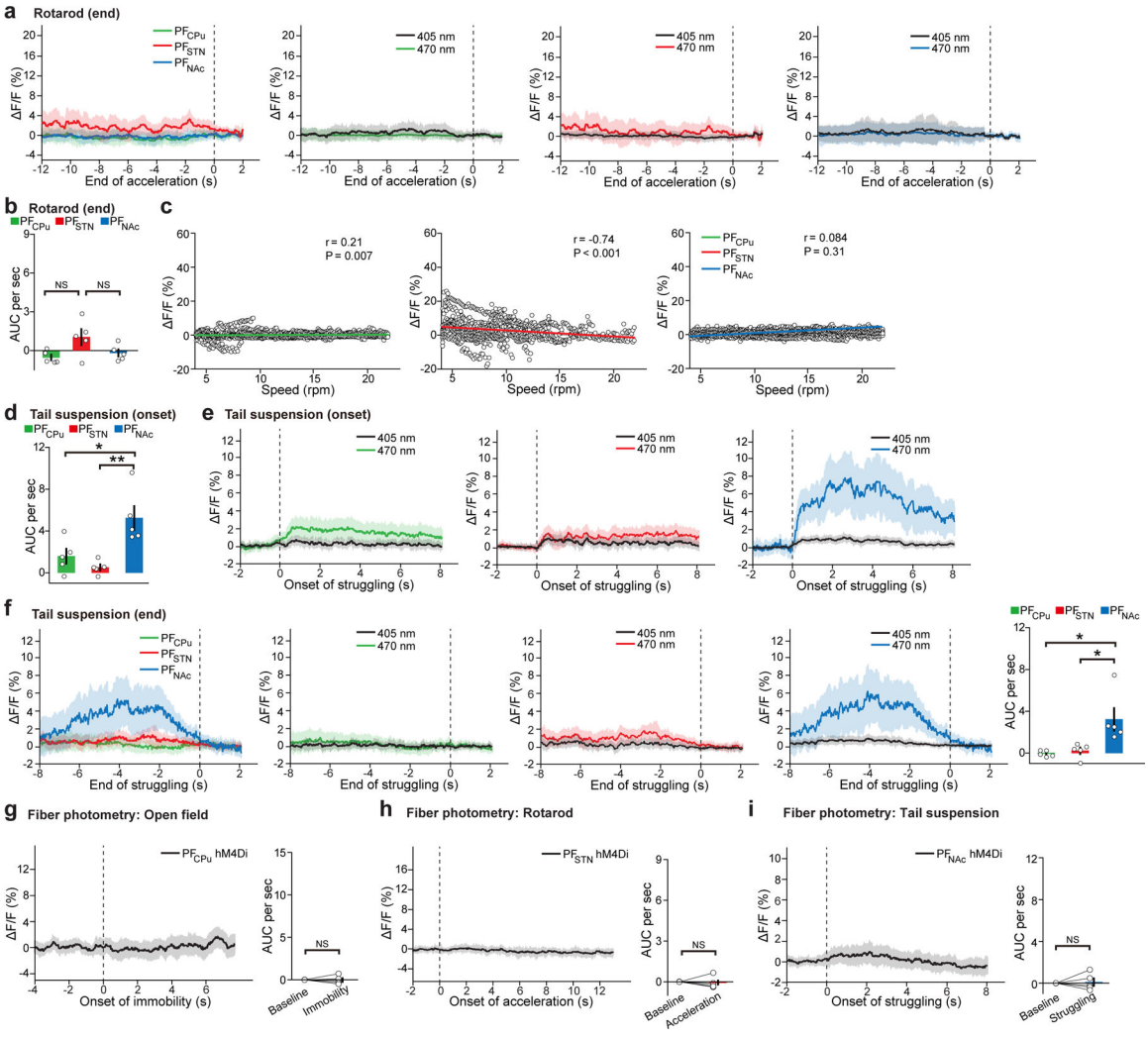


**Extended Data Fig. 6. *In vivo* fiber photometry analyses for the end of the acceleration epoch in rotarod and tail suspension recordings.**

**a**–**c**, Averaged fluorescence change and 405/470 nm traces for each PF population for rotarod recordings aligned to the end of acceleration (**a**), AUC per sec for rotarod aligned to the end of acceleration (−4 to 0 s compared to baseline 0 to 2 s) (**b**), correlation between fluorescence change and mouse speed (computed based on the speed of the rod) in the rotarod test (r, correlation coefficient) ($n$ = 5 mice per group) (**c**). **d**–**f**, AUC per sec for tail

suspension aligned to the onset of struggling (0 to 4 s compared to baseline −2 to 0 s) (**d**), 405 and 470 nm traces for each PF population for tail suspension recordings aligned to the onset of struggling (**e**), averaged fluorescence change and 405/470 nm traces aligned to the end of struggling, AUC per sec for tail suspension aligned to the end of struggling (−4 to 0 s compared to baseline 0 to 2 s) ($n = 5$ mice per group) (**f**). **g**–**i**, Averaged fluorescence change and AUC per sec for $PF_{CPu}$ hM4Di mice during open field (**g**), $PF_{STN}$ hM4Di mice during rotarod (**h**), and $PF_{NAc}$ hM4Di mice during tail suspension ($n = 5$ mice per group) (**i**). $PF_{CPu}$ hM4Di, $PF_{STN}$ hM4Di, and $PF_{NAc}$ hM4Di mice received a retrograde AAV expressing Cre in CPu, STN, or NAc, Cre-dependent GCaMP6s and hM4Di viruses in PF, followed by fibers placed above PF. Data are presented as mean ± SEM; $*P < 0.05$, $**P < 0.01$. NS, not significant. One-way ANOVA followed by Bonferroni post-hoc test (**b**, **d**, **f**) and two-tailed paired *t* test (**g**–**i**). $F = 3.95$, $P = 0.048$, $PF_{CPu}$ vs. $PF_{STN}$ $t = 2.68$, $PF_{STN}$ vs. $PF_{NAc}$ $t = 2.07$ (**b**), $F = 9.73$, $P = 0.003$, $PF_{CPu}$ vs. $PF_{NAc}$ $t = 3.25$, $PF_{STN}$ vs. $PF_{NAc}$ $t = 4.21$ (**d**), $F = 7.8$, $P = 0.0068$, $PF_{CPu}$ vs. $PF_{NAc}$ $t = 3.563$, $PF_{STN}$ vs. $PF_{NAc}$ $t = 3.258$ (**f**), $P = 0.87$ (**g**), $P = 0.74$ (**h**), $P = 0.8$ (**i**).

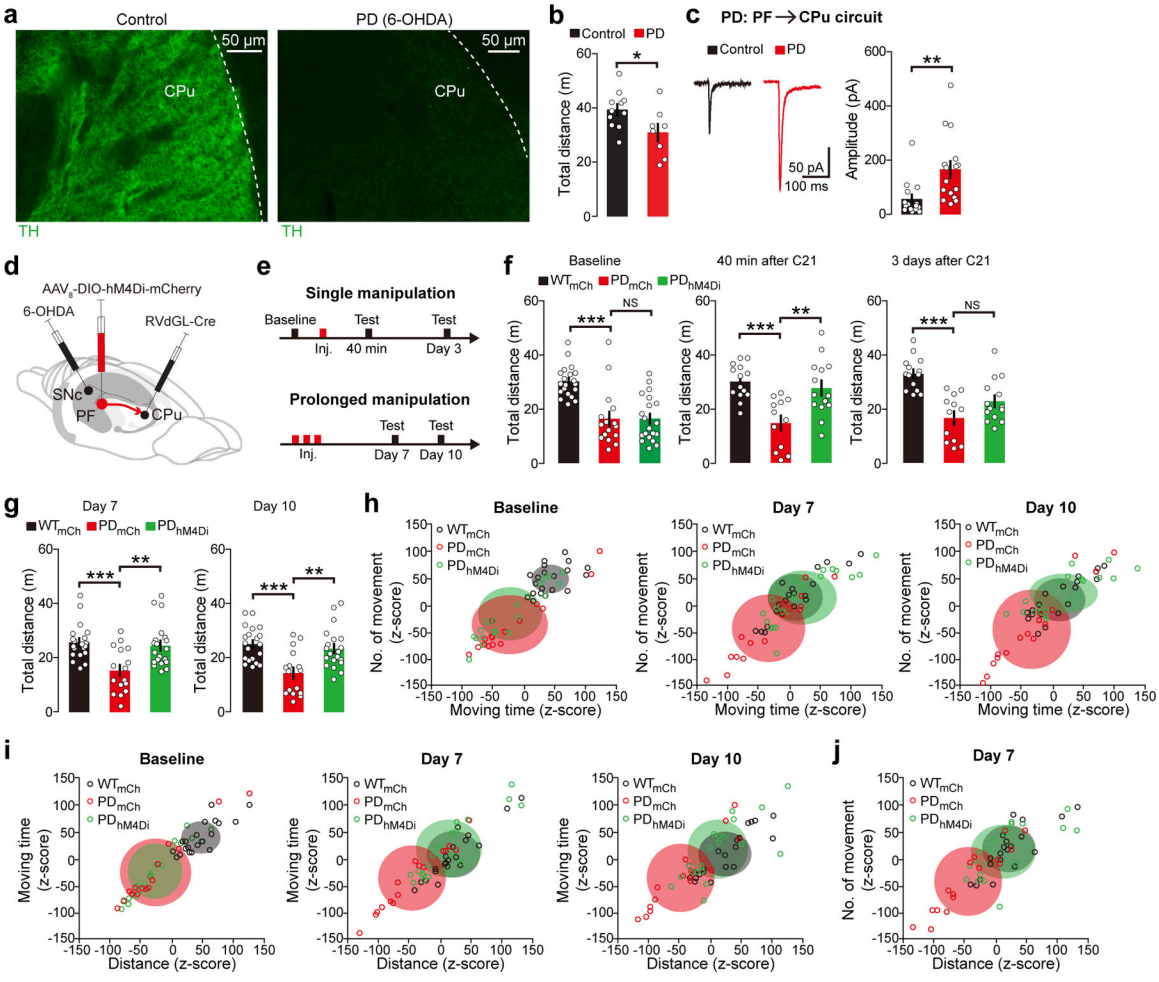


**Extended Data Fig. 7. Prolonged chemogenetic inhibition of $PF_{CPu}$ neurons rescued locomotion in PD model mice up to 10 days later.**

**a**, *TH* staining in CPu of saline control (left) or 6-OHDA-injected PD model (right) mice. **b**, Open field test using saline control and PD model mice 30 days after 6-OHDA injections ($n$ = 11 saline, $n$ = 8 PD model mice). **c**, Representative traces and evoked EPSC amplitudes recorded in CPu neurons receiving PF input from control and PD model mice (Control: $n$ = 15 neurons (5, 5, 5), PD: $n$ = 16 neurons (5, 6, 5) from 3 mice each). **d**, $PF_{CPu}$ inhibition in PD model mice by injecting a retrograde RVdGL-Cre in CPu, Cre-dependent hM4Di-mCh in PF, and 6-OHDA in SNc. **e**-**j**, Open arena behavior protocol using two different manipulation strategies starting from 14 days after 6-OHDA injections (**e**). For single manipulation experiments, total distance during a 20-min open arena test was measured prior to the C21 injection (Baseline), or 40 min and 3 days after one C21 injection (Test) (Baseline: $n$ = 20 $WT_{mCh}$, $n$ = 16 $PD_{mCh}$, $n$ = 20 $PD_{hM4Di}$ mice; 40 min and 3 days: $n$ = 14 $WT_{mCh}$, $n$ = 12 $PD_{mCh}$, $n$ = 14 $PD_{hM4Di}$ mice) (**f**). Saline was injected 40 min before the baseline session. For prolonged manipulation experiments, total distance, number of movements, and moving time (**g**-**j**) during tests were measured 7 days and 10 days after the 3-day prolonged C21 protocol (Day 7 and Day 10: $n$ = 20 $WT_{mCh}$, $n$ = 16 $PD_{mCh}$, $n$ = 20 $PD_{hM4Di}$ mice). In panels h and **i**, baseline data plotted from panel **f**. $WT_{mCh}$ mice were injected with a retrograde RVdGL-Cre injected in CPu, Cre-dependent mCh in PF, and saline in SNc. Day 7 data related to Fig. 4b (**j**). Data are presented as mean ± SEM; $^{**}P < 0.01$, $^{***}P < 0.001$. NS, not significant. Two-tailed unpaired $t$ test (**b**, **c**), and one-way ANOVA followed by Bonferroni post-hoc test (**f**, **g**). $P = 0.033$ (**b**), $P = 0.004$ (**c**), Baseline: $F = 17.77$, $P < 0.0001$, $WT_{mCh}$ vs. $PD_{mCh}$ $t = 5.26$, $PD_{mCh}$ vs. $PD_{hM4Di}$ $t = 0.006$, 40 min after C21: $F = 10.7$, $P = 0.0002$, $WT_{mCh}$ vs. $PD_{mCh}$ $t = 4.35$, $PD_{mCh}$ vs. $PD_{hM4Di}$ $t = 3.67$, 3 days after C21: $F = 15.35$, $P < 0.0001$, $WT_{mCh}$ vs. $PD_{mCh}$ $t = 5.44$, $PD_{mCh}$ vs. $PD_{hM4Di}$ $t = 2.06$ (**f**), Day 7: $F = 9.46$, $P = 0.0003$, $WT_{mCh}$ vs. $PD_{mCh}$ $t = 4.05$, $PD_{mCh}$ vs. $PD_{hM4Di}$ $t = 3.57$, Day 10: $F = 10.72$, $P = 0.0001$, $WT_{mCh}$ vs. $PD_{mCh}$ $t = 4.37$, $PD_{mCh}$ vs. $PD_{hM4Di}$ $t = 3.69$ (**g**).

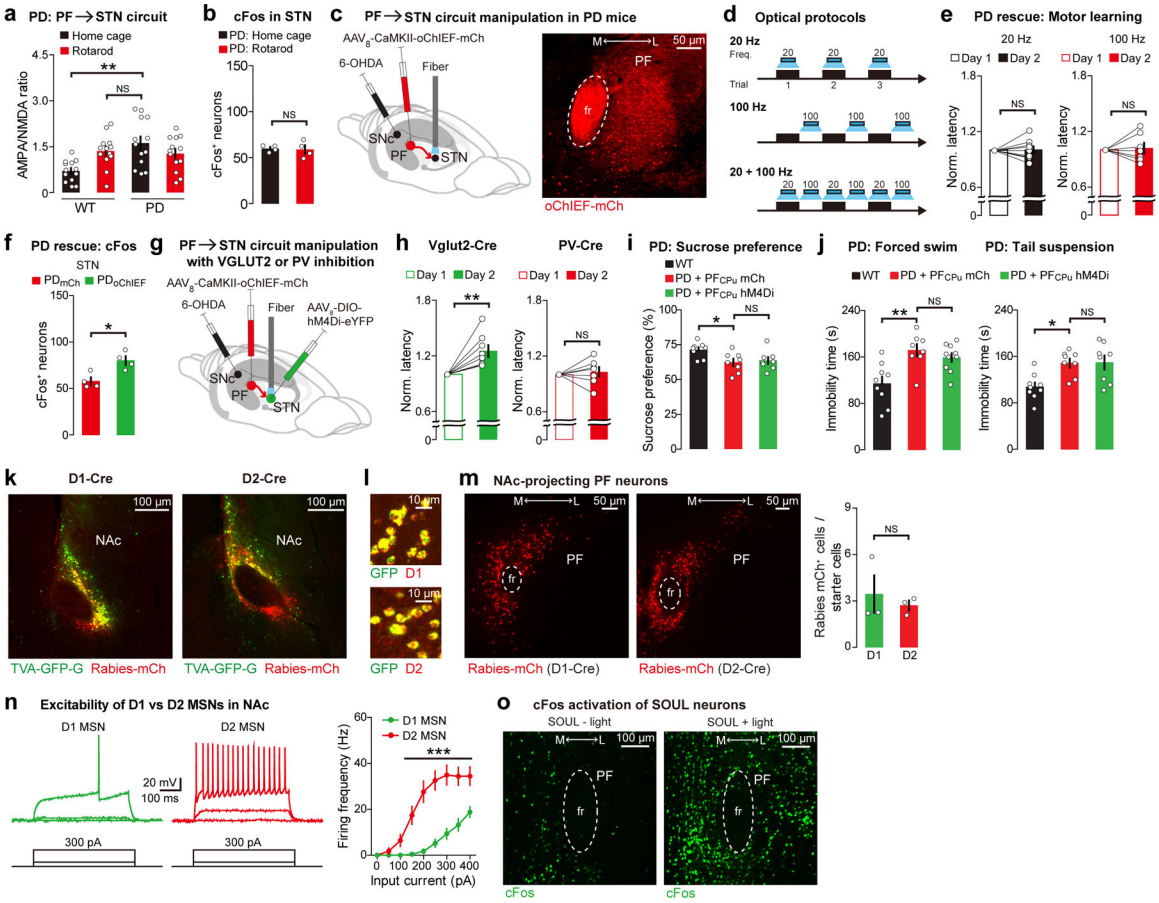


**Extended Data Fig. 8. Strengthening the PF→STN circuit restores motor learning in PD model mice through *PV*$^{+}$ STN neurons, and PD model mice show depression-like phenotypes.**

**a**, AMPA/NMDA ratio recordings of PF→STN circuit from WT and PD model mice in home cage and rotarod conditions (WT data from Fig. 2e, PD data from Fig. 4d). **b**, *cFos* activation of STN neurons using home cage and rotarod PD model mice ($n$ = 4 mice per group). **c**, PF→STN circuit manipulation in PD model mice by injecting CaMKII-oChIEF-mCh virus in PF, optic fibers above STN, and 6-OHDA injections in SNc (left). Expression of oChIEF-mCh in PF (right). **d**, Optical protocols including 20 Hz- and 100 Hz-only protocols. 20 Hz blue light was delivered during trials whereas 100 Hz blue light was delivered between trials. **e**, Activation of the PF→STN circuit in PD model mice using the 20 Hz or 100 Hz protocol during rotarod behavior (20 Hz: $n$ = 9, 100 Hz: $n$ = 7 mice). **f**, STN *cFos* activation in PD model mice ($n$ = 4 mice per group) following PF→STN circuit activation with the 20 + 100 Hz protocol during rotarod. Control PD model mice ($PD_{mCh}$) was prepared similar to the $PD_{oChIEF}$ mice except that a mCh virus was injected in PF. **g-h**, PF→STN circuit strengthening with *VGLUT2* or *PV* inhibition in STN during rotarod, using PD model mice. CaMKII-oChIEF-mCh virus was injected in PF, Cre-dependent hM4Di virus in STN, 6-OHDA in SNc, and fibers targeted STN of Vglut2-Cre or PV-Cre mice (**g**). Rotarod behavior ($n$ = 8 Vglut2-Cre, $n$ = 7 PV-Cre mice) (**h**). **i-j**, Sucrose preference ($n$ = 8 mice per group) (**i**) and total immobility time in forced swim ($n$ = 9 WT, $n$ = 8 PD + $PF_{CPu}$ mCh, $n$ = 10 PD + $PF_{CPu}$ hM4Di mice) and tail

suspension ($n$ = 9 WT, $n$ = 8 PD + $PF_{CPu}$ mCh, $n$ = 8 PD + $PF_{CPu}$ hM4Di mice) tests in PD (**j**). To rule out the possibility that decreased locomotion of PD model mice resulted in their performance in these assays, a retrograde RVdGL-Cre was injected in CPu and Cre-dependent hM4Di-mCh was injected in PF of PD model mice (PD + $PF_{CPu}$ hM4Di group). For WT and PD + $PF_{CPu}$ mCh groups, Cre-dependent mCh was injected in PF in place of the hM4Di virus. C21 was injected 40 min before tests to rescue locomotion deficits in PD model mice by manipulating the PF→CPu circuit. **k**-**m**, Monosynaptic retrograde RV tracing from $D1^+$ or $D2^+$ NAc neurons. Images show starter cells in NAc (**k**), FISH co-staining of *GFP* with *D1* or *D2* (**l**), and corresponding PF labeling ($n$ = 3 mice per group) (**m**). **n**, Representative traces (left) and current-frequency curves (right) of *ex vivo* recordings from $D2^-$ (putative $D1^+$) or $D2^+$ MSNs in NAc using D2-eGFP mice (*D1*: $n$ = 20 neurons (6, 7, 7), *D2*: $n$ = 16 neurons (6, 4, 6) from 3 mice each). **o**, Representative images of PF sections stained with *cFos* from mice expressing SOUL in PF neurons, including a no light group (SOUL - light) and a 5 min light activated group (SOUL + light) in the home cage. Data are presented as mean ± SEM; *$P$ < 0.05, **$P$ < 0.01, ***$P$ < 0.001. NS, not significant. One-way ANOVA followed by Bonferroni post-hoc test (**a**), two-tailed unpaired $t$ test (**b**, **f**, **m**), two-tailed paired $t$ test (**e**, **h**), and two-way ANOVA with repeated measures followed by Bonferroni post-hoc test (**n**). $F$ = 5.81, $P$ = 0.0018, Home cage WT vs. home cage PD $t$ = 4.04, Rotarod WT vs. Home cage PD $t$ = 1.15 (**a**), $P$ = 0.84 (**b**), 20 Hz $P$ = 0.87, 100 Hz $P$ = 0.72 (**e**), $P$ = 0.012 (**f**), Vglut2-Cre $P$ = 0.005, PV-Cre $P$ = 0.59 (**h**), $F$ = 4.28, $P$ = 0.028, WT vs. PD + $PF_{CPu}$ mCh $t$ = 2.71, PD + $PF_{CPu}$ mCh vs. PD + $PF_{CPu}$ hM4Di $t$ = 0.39 (**i**), Forced swim: $F$ = 8.92, $P$ = 0.0013, WT vs. PD + $PF_{CPu}$ mCh $t$ = 3.95, PD + $PF_{CPu}$ mCh vs. PD + $PF_{CPu}$ hM4Di $t$ = 0.88, Tail suspension: $F$ = 7.18, $P$ = 0.004, WT vs. PD + $PF_{CPu}$ mCh $t$ = 3.21, PD + $PF_{CPu}$ mCh vs. PD + $PF_{CPu}$ hM4Di $t$ = 0.07 (**j**), $P$ = 0.58 (**m**), $F$ = 38.34, DFn = 1, DFd = 272, $P$ < 0.0001 (**n**).

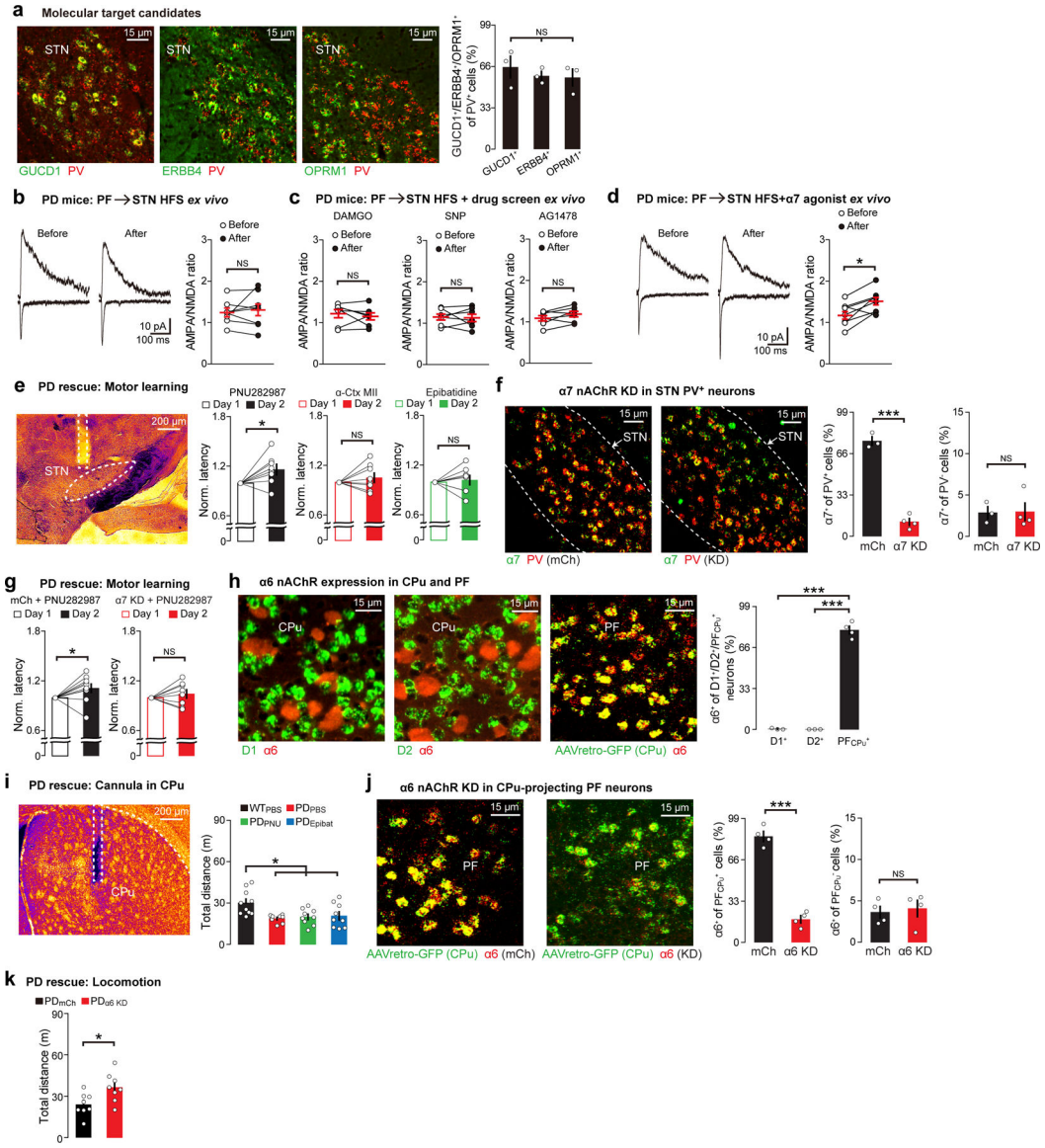


**Extended Data Fig. 9. Testing molecular target candidates in the PF→STN and PF→CPu circuits.**

**a**, *GUCD1* (guanylyl cyclase gene, the *NO* receptor), *ERBB4*, and *OPRM1* (μ-opioid receptor gene) FISH staining with *PV* in STN sections. 65.6% of all $PV^+$ neurons were $GUCD1^+$, 58.5% of all $PV^+$ neurons were $ERBB4^+$, 57.2% of all $PV^+$ neurons were $OPRM1^+$ ($n$ = 3 mice per group). **b**, AMPA/NMDA ratio recordings of the PF→STN circuit, specifically $PV^+$ STN neurons, before and after optical high frequency stimulation (HFS) in PD model mice ($n$ = 8 neurons (2, 3, 3) from 3 mice). oChIEF-mCh virus was injected in PF, Cre-dependent eYFP virus in STN, and 6-OHDA in SNc of PV-Cre mice. **c**-**d**, With DAMGO (μ-opioid receptor agonist), SNP (*NO* receptor agonist), AG1478 (*ERBB4* receptor antagonist) (**c**) or PNU282987 (*α7* agonist) (**d**) bath application, AMPA/NMDA ratio recordings of the PF→$STN_{PV}$ circuit before and after optical HFS in PD model mice (DAMGO: $n$ = 7 neurons (2, 2, 3), SNP: $n$ = 7 neurons (3, 2, 2), AG1478: $n$ = 7 neurons (2, 2, 3), PNU282987: $n$ = 8 neurons (2, 3, 3) from 3 mice each). oChIEF-mCh virus was

injected in PF, Cre-dependent eYFP virus in STN, and 6-OHDA in SNc of PV-Cre mice. **e**, Local bilateral infusion of PNU282987, α-Ctx MII, or epibatidine into STN of PD model mice prior to rotarod behavior assays ($n$ = 8 mice per group). **f**, $\alpha7$ nAChRs FISH staining with $PV$ in STN sections from mCh and KD mice, $\alpha7$ in $PV^+$ cells is decreased by 84% in KD mice as compared to mCh controls ($n$ = 3 mCh, $n$ = 4 $\alpha7$KD mice). **g**, Activating $\alpha7$ nAChRs without (left) or with (right) $\alpha7$KD from $PV^+$ STN neurons during rotarod, using PD model mice ($n$ = 10 mCh, $n$ = 8 $\alpha7$KD mice). $PD_{\alpha7\ KD}$ received a Cre-dependent Cas9 and gRNA viruses (for knockdown of $\alpha7$ nAChRs) and cannula implants above STN, and 6-OHDA in SNc of PV-Cre mice. **h**, $\alpha6$ nAChRs FISH staining with $D1$ or $D2$ in mouse CPu sections and with $PF_{CPu}$ neurons in mouse PF sections. $PF_{CPu}$ neurons were labeled by injecting AAVretro-GFP in CPu ($n$ = 3 $D1^+$, $n$ = 3 $D2^+$, $n$ = 4 $PF_{CPu}^+$ mice). **i**, Representative cannula implant targeting CPu for local infusion experiments (left), local bilateral infusion of PBS, PNU282987, or epibatidine into CPu of PD model mice and infusion of PBS into CPu of WT mice prior to open field behavior ($n$ = 10 $WT_{PBS}$, 9 $PD_{PBS}$, 9 $PD_{PNU}$, 9 $PD_{Epibat}$ mice) (right). $WT_{PBS}$ and $PD_{PBS}$ data from Fig. 5e. **j**, $\alpha6$ nAChRs FISH staining with $PF_{CPu}$ neurons in PF sections from mCh and KD mice, $\alpha6$ in $PF_{CPu}^+$ cells is decreased by 78% in KD mice as compared to mCh controls ($n$ = 4 mice per group). **k**, Total distance mice travelled in the open field after KD of $\alpha6$ in $PF_{CPu}$ neurons of PD model mice ($n$ = 8 mice per group). $PD_{\alpha6\ KD}$ received a retrograde RVdGL-Cre in CPu, Cre-dependent Cas9 and gRNA viruses (for knockdown of $\alpha6$ nAChRs) in $PF_{CPu}$ neurons, and 6-OHDA in SNc. Data are presented as mean ± SEM; *$P$ < 0.05, ***$P$ < 0.001. NS, not significant. One-way ANOVA followed by Bonferroni post-hoc test (**a**, **h**, **i**), two-tailed paired $t$ test (**b**-**e**, **g**), and two-tailed unpaired $t$ test (**f**, **j**, **k**). $F$ = 0.45, $P$ = 0.13 (**a**), $P$ = 0.60 (**b**), DAMGO $P$ = 0.48, SNP $P$ = 0.82, AG1478 $P$ = 0.12 (**c**), $P$ = 0.011 (**d**), PNU282987 $P$ = 0.034, α-Ctx MII $P$ = 0.34, Epibatidine $P$ = 0.66 (**e**), $P$ < 0.0001 (**f**), mCh + PNU282987 $P$ = 0.04, $\alpha7$KD + PNU282987 $P$ = 0.37 (**g**), $F$ = 456.9, $P$ < 0.0001, $D1^+$ vs. $PF_{CPu}^+$ $t$ = 25.49, $D2^+$ vs. $PF_{CPu}^+$ $t$ = 25.6 (**h**), $F$ = 5.16, $P$ = 0.0049, $WT_{PBS}$ vs. $PD_{PBS}$ $t$ = 3.45, $WT_{PBS}$ vs. $PD_{PNU}$ $t$ = 3.09, $WT_{PBS}$ vs. $PD_{Epibat}$ $t$ = 2.86 (**i**), $P$ < 0.0001 (**j**), $P$ = 0.02 (**k**).

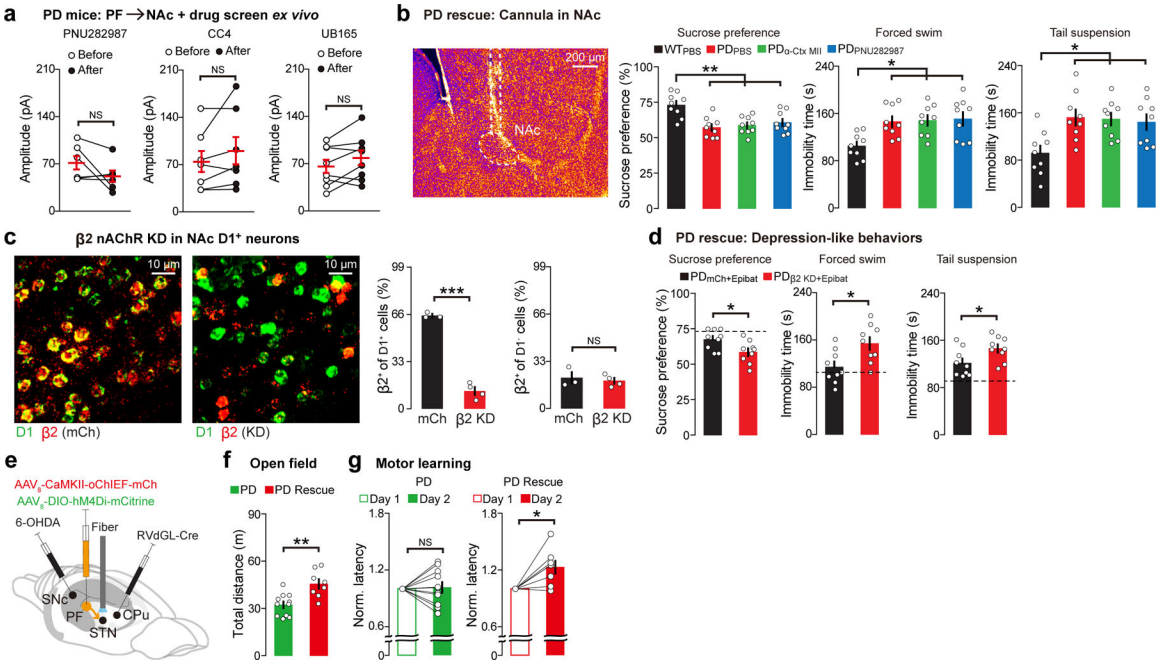


**Extended Data Fig. 10. Testing molecular target candidates in the PF→NAc circuit, and rescue of motor phenotypes in the same mice using $PF_{CPu}$ cell body and PF→STN circuit manipulations *in vivo*.**

**a**, Before and after bath application of PNU282987 (*α7* agonist), CC4 (*α6* agonist), and UB165 (*α3* agonist), evoked EPSCs were recorded from *D1* MSNs in NAc of PD model mice. oChIEF-mCh virus was injected in PF and 6-OHDA in SNc of D2-eGFP mice (PNU282987: $n = 6$ neurons (1, 2, 1, 1, 1), CC4: $n = 7$ neurons (1, 2, 1, 1, 2), UB165: $n = 8$ neurons (2, 2, 1, 2, 1) from 5 mice each). **b**, Representative cannula implant targeting NAc for local infusion experiments (left), local bilateral infusion of PBS, α-Ctx MII, or PNU282987 into NAc of PD model mice and infusion of PBS into NAc of WT mice prior to depression-like behavior tests ($n = 9$ mice per group) (right). $WT_{PBS}$ and $PD_{PBS}$ data from Fig. 5h. **c**, *β2* nAChRs FISH staining with *D1* in NAc sections from mCh and KD mice, *β2* in $D1^+$ cells is decreased by 80% in KD mice as compared to mCh controls ($n = 3$ mCh, $n = 4$ *β2* KD mice). **d**, Activating *β2* nAChRs without ($PD_{mCh+Epibat}$) or with ($PD_{β2\ KD+Epibat}$) *β2* KD from $D1^+$ NAc neurons during depression-like behaviors, using PD model mice ($n = 9$ mice per group). Dashed line indicates WT level from Fig. 5h. $PD_{β2\ KD}$ received a Cre-dependent Cas9 and gRNA viruses (for knockdown of *β2* nAChRs), cannula implants in NAc, and 6-OHDA in SNc of D1-Cre mice. **e**, A retrograde RVdGL-Cre was injected in CPu, Cre-dependent hM4Di-mCitrine (for $PF_{CPu}$ labeling), and CaMKII-oChIEF-mCh (for STN terminal manipulations) in PF, optic fibers targeting STN, and 6-OHDA injected in SNc. **f**, Total distance in the open field was measured 40 min after C21 injections. PD model mice that received 6-OHDA injections in SNc without any subsequent PF manipulation was the baseline group (labeled PD). PD model mice with $PF_{CPu}$ manipulations are referred to as PD Rescue ($n = 11$ PD, $n = 8$ PD Rescue mice). **g**, Rotarod tests were performed after the open field paradigm. For rotarod, PF→STN circuit strengthening using our optical LTP protocol (20 + 100 Hz) was performed ($n = 11$ PD, $n = 8$ PD Rescue mice). Data are presented as mean ± SEM; $*P < 0.05$, $**P < 0.01$, $***P < 0.001$. NS, not significant.

Two-tailed paired *t* test (**a**, **g**), one-way ANOVA followed by Bonferroni post-hoc test (**b**), and two-tailed unpaired *t* test (**c**, **d**, **f**). PNU282987 $P = 0.14$, CC4 $P = 0.17$, UB165 $P = 0.10$ (**a**), Sucrose preference: $F = 8.71$, $P = 0.0002$, $WT_{PBS}$ vs. $PD_{PBS}$ $t = 4.57$, $WT_{PBS}$ vs. $PD_{\alpha\text{-Ctx MII}}$ $t = 4.14$, $WT_{PBS}$ vs. $PD_{PNU282987}$ $t = 3.57$, Forced swim: $F = 5.59$, $P = 0.0034$, $WT_{PBS}$ vs. $PD_{PBS}$ $t = 3.16$, $WT_{PBS}$ vs. $PD_{\alpha\text{-Ctx MII}}$ $t = 3.32$, $WT_{PBS}$ vs. $PD_{PNU282987}$ $t = 3.52$, Tail suspension: $F = 5.32$, $P = 0.0044$, $WT_{PBS}$ vs. $PD_{PBS}$ $t = 3.44$, $WT_{PBS}$ vs. $PD_{\alpha\text{-Ctx MII}}$ $t = 3.28$, $WT_{PBS}$ vs. $PD_{PNU282987}$ $t = 2.99$ (**b**), $P < 0.0001$ (**c**), Sucrose preference $P = 0.022$, Forced swim $P = 0.012$, Tail suspension $P = 0.029$ (**d**), $P = 0.0017$ (**f**), PD $P = 0.78$, PD Rescue $P = 0.011$ (**g**).

## Acknowledgments

We thank X. Gong and J. Ting for generating the Cre-dependent SOUL construct; C. Wang for viral packaging; M. Fleishman, B. Clear, J. Kim, and H. Zaniewski for technical assistance; Z. Yang and W. Chen for data analysis; and all members of the Feng laboratory for their support. The J. Douglas Tan Fellowship supported Y.Z. The Warren Alpert Distinguished Scholar Award and NIH 1K99NS125121-01 supported D.R. This work was supported by the Stanley Center for Psychiatric Research at the Broad Institute of MIT and Harvard, Hock E. Tan and K. Lisa Yang Center for Autism Research at MIT, James and Patricia Poitras Center for Psychiatric Disorders Research at MIT, and NIH BRAIN Initiative (U01MH114819) (to G.F.).

## Data availability

All figures in which statistical comparisons are indicated in the legend and/or methods include individual biological data points reported for each main and extended data figure panel along with P values. For the entire manuscript, a source data file has been provided. Reagents are available from the corresponding authors upon reasonable request.

## References

1. Albin RL, Young AB & Penney JB The functional anatomy of basal ganglia disorders. Trends Neurosci. 12, 366–375 (1989). [PubMed: 2479133]
2. The Parkinson Study Group, Levodopa and the progression of Parkinson's disease. N. Engl. J. Med 351, 2498–2508 (2004). [PubMed: 15590952]
3. Hamani C, Saint-Cyr JA, Fraser J, Kaplitt M & Lozano AM The subthalamic nucleus in the context of movement disorders. Brain 127, 4–20 (2004). [PubMed: 14607789]
4. Smiley-Oyen AL, Worringham CJ & Cross CL Motor learning processes in a movement-scaling task in olivopontocerebellar atrophy and Parkinson's disease. Exp. Brain Res 152, 453–465 (2003). [PubMed: 12898095]
5. Marinelli L, Quartarone A, Hallett M, Frazzitta G & Ghilardi MF The many facets of motor learning and their relevance for Parkinson's disease. Clin. Neurophysiol 128, 1127–1141 (2017). [PubMed: 28511125]
6. Poewe W Non-motor symptoms in Parkinson's disease. Eur. J. Neurol 15, 14–20 (2008). [PubMed: 18353132]
7. Saalmann YB Intralaminar and medial thalamic influence on cortical synchrony, information transmission, and cognition. Front. Syst. Neurosci 8, 83 (2014). [PubMed: 24847225]
8. Smith Y, Raju DV, Pare JF & Sidibe M The thalamostriatal sytem: a highly specific network of the basal ganglia circuitry. Trends Neurosci. 27, 520–527 (2004). [PubMed: 15331233]
9. Brown HD, Baker PM & Ragozzino ME The parafascicular thalamic nucleus concomitantly influences behavioral flexibility and dorsomedial striatal acetylcholine output in rats. J. Neurosci 30, 14390–14398 (2010). [PubMed: 20980596]
10. Diaz-Hernandez E et al. The thalamostriatal projections contribute to the initiation and execution of a sequence of movements. Neuron 100, 739–752 (2018). [PubMed: 30344045]

11. Jouve L, Salin P, Melon C & Kerkerian-Le Goff L Deep brain stimulation of the center median-parafascicular complex of the thalamus has efficient anti-parkinsonian action associated with widespread cellular responses in the basal ganglia network in a rat model of Parkinson's disease. J. Neurosci 30, 9919–9928 (2010). [PubMed: 20660274]
12. Berendse HW & Groenewegen HJ Organization of the thalamostriatal projections in the rat, with special emphasis on the ventral striatum. J. Comp. Neurol 299, 187–228 (1990). [PubMed: 2172326]
13. Heshmati M & Russo SJ Anhedonia and the brain reward circuitry in depression. Curr. Behav. Neurosci. Rep 2, 146–153 (2015). [PubMed: 26525751]
14. Smith Y & Parent A Differential connections of caudate nucleus and putamen in the squirrel monkey (*Saimiri sciureus*). Neuroscience 18, 347–371 (1986). [PubMed: 3736862]
15. Kita T, Shigematsu N & Kita H Intralaminar and tectal projections to the subthalamus in the rat. Eur. J. Neurosci 44, 2899–2908 (2016). [PubMed: 27717088]
16. Mouroux M, Hassani OK & Feger J Electrophysiological study of the excitatory parafascicular projection to the subthalamic nucleus and evidence for ipsi- and contralateral controls. Neuroscience 67, 399–407 (1995). [PubMed: 7675175]
17. Wickersham IR, Sullivan HA & Seung HS Axonal and subcellular labelling using modified rabies viral vectors. Nat. Commun 4, 2332–2332 (2013). [PubMed: 23945836]
18. Chatterjee S et al. Nontoxic, double-deletion-mutant rabies viral vectors for retrograde targeting of projection neurons. Nat. Neurosci 21, 638–646 (2018). [PubMed: 29507411]
19. Thompson KJ et al. DREADD agonist 21 is an effective agonist for muscarinic-based DREADDs in vitro and in vivo. ACS Pharmacol. Transl. Sci 1, 61–72 (2018). [PubMed: 30868140]
20. Parker PRL, Lalive AL & Kreitzer AC Pathway-specific remodeling of thalamostriatal synapses in parkinsonian mice. Neuron 89, 734–740 (2016). [PubMed: 26833136]
21. Luh LM, Das I & Bertolotti A qMotor, a set of rules for sensitive, robust and quantitative measurements of motor performances in mice. Nat. Protoc 12, 1451–1457 (2017). [PubMed: 28686587]
22. Voorn P, Vanderschuren LJ, Groenewegen HJ, Robbins TW & Pennartz CM Putting a spin on the dorsal-ventral divide of the striatum. Trends Neurosci. 27, 468–74 (2004). [PubMed: 15271494]
23. Wickersham IR et al. Monosynaptic restriction of transsynaptic tracing from single, genetically targeted neurons. Neuron 53, 639–647 (2007). [PubMed: 17329205]
24. Barroso-Chinea P et al. Expression of the mRNAs encoding for the vesicular glutamate transporters 1 and 2 in the rat thalamus. J. Comp. Neurol 5, 703–715 (2007).
25. Parolari L, Schneeberger M, Heintz N & Friedman JM Functional analysis of distinct populations of subthalamic nucleus neurons on Parkinson's disease and OCD-like behaviors in mice. bioRxiv 137679 [Preprint]. 11 June 2020.
26. Hontanilla B, Parent A & Gimenez-Amaya JM Parvalbumin and calbindin D-28k in the entopeduncular nucleus, subthalamic nucleus, and substantia nigra of the rat as revealed by double-immunohistochemical methods. Synapse 4, 359–367 (1997).
27. Levesque JC & Parent A GABAergic interneurons in human subthalamic nucleus. Mov. Disord 5, 574–584 (2005).
28. Ferguson BR & Gao WJ PV interneurons: Critical regulators of E/I balances for prefrontal cortex-dependent behavior and psychiatric disorders. Front. Neural Circuits 12, 37 (2018). [PubMed: 29867371]
29. Smith Y & Parent A Neurons of the subthalamic nucleus in primates display glutamate but not GABA immunoreactivity. Brain Res. 453, 353–356 (1988). [PubMed: 2900056]
30. Emmi A, Antonini A, Macchi V, Porzionato A & De Caro R Anatomy and connectivity of the subthalamic nucleus in humans and non-human primates. Front. Neuroanat 14, 13 (2020). [PubMed: 32390807]
31. Zhang Y et al. MeCP2 in cholinergic interneurons of nucleus accumbens regulates fear learning. Elife 9, e55342. [PubMed: 32420873]
32. Deumens R, Blokland A & Prickaerts J Modeling Parkinson's disease in rats: An evaluation of 6-OHDA lesions of the nigrostriatal pathway. Exp. Neurol 175, 303–317 (2002). [PubMed: 12061862]

33. Carvalho MM et al. Behavioral characterization of the 6-hydroxydopamine model of Parkinson's disease and pharmacological rescuing of non-motor deficits. Mol. Neurodegener 8, 14 (2013). [PubMed: 23621954]
34. Nabavi S et al. Engineering a memory with LTD and LTP. Nature 511, 348–352 (2014). [PubMed: 24896183]
35. Roy DS et al. Memory retrieval by activating engram cells in mouse models of early Alzheimer's disease. Nature 531, 508–512 (2016). [PubMed: 26982728]
36. Gong X et al. An ultra-sensitive step-function opsin for minimally invasive optogenetic stimulation in mice and macaques. Neuron 107, 38–51 (2020). [PubMed: 32353253]
37. Lein ES et al. Genome-wide atlas of gene expression in the adult mouse brain. Nature 445, 168–176 (2007). [PubMed: 17151600]
38. Feduccia AA, Chatterjee S & Bartlett SE Neuronal nicotinic acetylcholine receptors: neuroplastic changes underlying alcohol and nicotine addictions. Front. Mol. Neurosci 5, 83 (2012). [PubMed: 22876217]
39. Pettorossi VE & Grassi S Different contributions of platelet-activating factor and nitric oxide in long-term potentiation of the rat medial vestibular nuclei. Acta Otolaryngol. Suppl 545, 160–165 (2001). [PubMed: 11677732]
40. Pitcher GM, Beggs S, Woo RS, Mei L & Salter MW ErbB4 is a suppressor of long-term potentiation in the adult hippocampus. Neuroreport 19, 139–143 (2008). [PubMed: 18185097]
41. Derrick BE & Martinez JL Opioid receptor activation is one factor underlying the frequency dependence of mossy fiber LTP induction. J. Neurosci 14, 4359–4367 (1994). [PubMed: 7913121]
42. Hajos M et al. The selective alpha7 nicotinic acetylcholine receptor agonist PNU-282987 [N-[(3R)-1-Azabicyclo[2.2.2]oct-3-yl]-4-chlorobenzamide hydrochloride] enhances GABAergic synaptic activity in brain slices and restores auditory gating deficits in anesthetized rats. J. Pharmacol. Exp. Ther 312, 1213–1222 (2005). [PubMed: 15523001]
43. Roy DS et al. Anterior thalamic dysfunction underlies cognitive deficits in a subset of neuropsychiatric disease models. Neuron 109, 2590–2603 (2021). [PubMed: 34197733]
44. Tanimura A, Du Y, Kondapalli J, Wokosin DL & Surmeier DJ Cholinergic interneurons amplify thalamostriatal excitation of striatal indirect pathway neurons in Parkinson's disease models. Neuron 101, 444–458 (2019). [PubMed: 30658860]
45. McIntosh JM et al. Analogs of alpha-conotoxin MII are selective for alpha6-containing nicotinic acetylcholine receptors. Mol. Pharmacol 65, 944–52 (2004). [PubMed: 15044624]
46. Beatty JA, Sylwestrak EL & Cox CL Two distinct populations of projection neurons in the rat lateral parafascicular thalamic nucleus and their cholinergic responsiveness. Neuroscience 162, 155–173 (2009). [PubMed: 19393292]
47. Mandelbaum G et al. Distinct cortical-thalamic-striatal circuits through the parafascicular nucleus. Neuron 102, 636–652 (2019). [PubMed: 30905392]
48. Klawonn AM & Malenka RC Nucleus accumbens modulation in reward and aversion. Cold Spring Harb. Symp. Quant. Biol 83, 119–129 (2018). [PubMed: 30674650]
49. Nelson AB & Kreitzer AC Reassessing models of basal ganglia function and dysfunction. Annu. Rev. Neurosci 37, 117–35 (2014). [PubMed: 25032493]
50. Watson GDR et al. Thalamic projections to the subthalamic nucleus contribute to movement initiation and rescue of parkinsonian symptoms. Sci. Adv 7, eabe9192 (2021). [PubMed: 33547085]
51. Kondoh K et al. A specific area of olfactory cortex involved in stress hormone responses to predator odours. Nature 532, 103–106 (2016). [PubMed: 27001694]
52. Liu K et al. Lhx6-positive GABA-releasing neurons of the zona incerta promote sleep. Nature 548, 582–587 (2017). [PubMed: 28847002]
53. Makara JK et al. Involvement of nitric oxide in depolarization-induced suppression of inhibition in hippocampal pyramidal cells during activation of cholinergic receptors. J. Neurosci 27, 10211–10222 (2007). [PubMed: 17881527]
54. Pitcher GM et al. Schizophrenia susceptibility pathway neuregulin 1-ErbB4 suppresses Src upregulation of NMDA receptors. Nat. Med 17, 470–478 (2011). [PubMed: 21441918]

55. Matsuyama S & Matsumoto A Epibatidine induces long-term potentiation (LTP) via activation of alpha4beta2 nicotinic acetylcholine receptors (nAChRs) in vivo in the intact mouse dentate gyrus: both alpha7 and alpha4beta2 nAChRs essential to nicotinic LTP. J. Pharmacol. Sci 93, 180–187 (2003). [PubMed: 14578586]

56. Fu W & Jhamandas JH Beta-amyloid peptide activates non-alpha7 nicotinic acetylcholine receptors in rat basal forebrain neurons. J. Neurophysiol 90, 3130–3136 (2003). [PubMed: 12890800]

57. Sala M et al. CC4, a dimer of cytisine, is a selective partial agonist at α4β2/α6β2 nAChR with improved selectivity for tobacco smoking cessation. Br. J. Pharmacol 168, 835–849 (2013). [PubMed: 22957729]

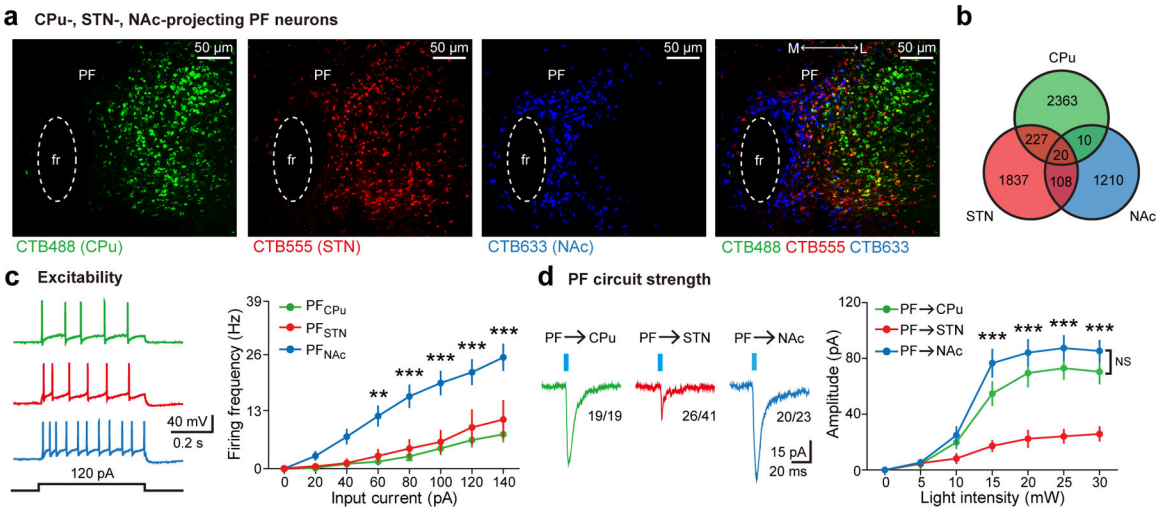


**Fig. 1. Three distinct projection-specific subpopulations in PF thalamus.**

**a**, Retrograde labeling of PF by injecting cholera toxin subunit B (CTB) into CPu, STN, or NAc. Medial (M) to lateral (L). **b**, A Venn diagram reflecting the overlap between CPu-, STN-, and NAc-projecting PF neurons ($n$ = 4 mice). 0.35% of all retrogradely-labeled cells in PF send collaterals to the three downstream targets. **c**, Representative traces (left) and *ex vivo* current-frequency recordings (right) of $PF_{CPu}$, $PF_{NAc}$, and $PF_{STN}$ neurons, which were labeled using retrograde rabies virus (RV) injected into CPu, NAc, or STN respectively ($PF_{CPu}$: $n$ = 19 neurons (5, 7, 7), $PF_{STN}$: $n$ = 15 neurons (6, 5, 4),$PF_{NAc}$: $n$ = 17 neurons (6, 7, 4) from 3 mice each). **d**, ChR2-eYFP virus was injected in PF and *ex vivo* recordings were performed from CPu, STN, and NAc. Representative traces (left, 20 mW light intensity) and quantification (right) of evoked EPSC amplitudes in response to graded light intensity stimulation (PF→CPu: $n$ = 15 neurons (5, 5, 5), PF→STN: $n$ = 15 neurons (4, 6, 5), PF→NAc: $n$ = 15 neurons (5, 5, 5) from 3 mice each). Data are presented as mean ± SEM; $^{**}P < 0.01$, $^{***}P < 0.001$. NS, not significant. Two-sided two-way ANOVA with repeated measures followed by Bonferroni post-hoc test (**c**, **d**). $F$ = 12.87, DFn = 2, DFd = 336, $P < 0.0001$ (**c**), $F$ = 31.54, DFn = 2, DFd = 252, $P < 0.0001$ (**d**).

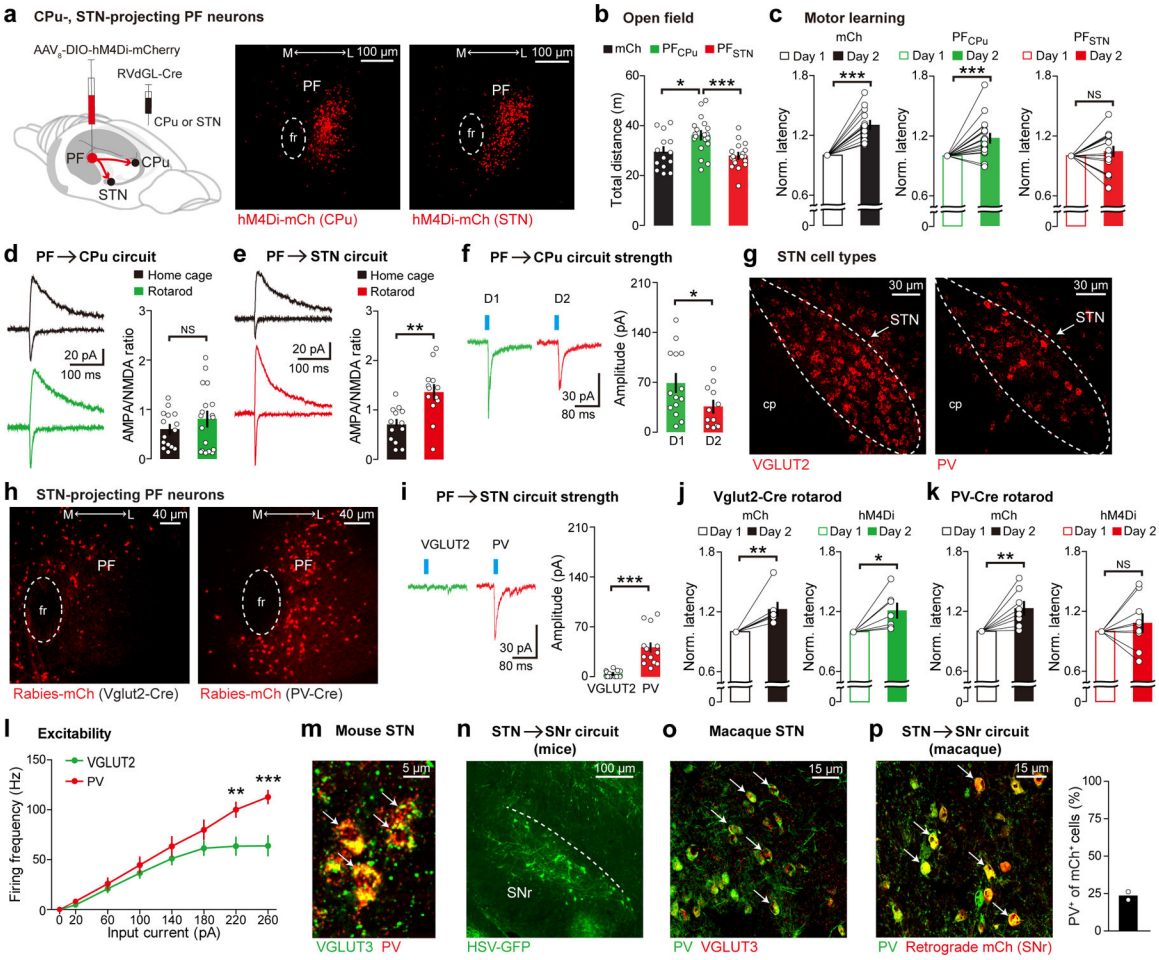


**Fig. 2. CPu- and STN-projecting PF neurons mediate different motor behaviors.**

**a**, hM4Di expression. **b-c**, Open field (**b**), rotarod (**c**) ($n = 14$ mCh, $n = 19$ $PF_{CPu}$, $n = 18$ $PF_{STN}$ mice). **d-e**, PF→CPu (Home: $n = 15$ (5, 5, 5), Rotarod: $n = 18$ (6, 6, 6), 3 mice) (**d**), PF→STN (Home: $n = 13$ (5, 4, 4), Rotarod: $n = 13$ neurons (4, 4, 5), 3 mice) e). **f**, EPSCs (*D1*: $n = 14$ (4, 4, 3, 3), *D2*: $n = 12$ neurons (3, 2, 4, 3), 4 mice). **g**, FISH. **h**, RV tracing. **i**, EPSCs (*VGLUT2*: $n = 15$ (4, 4, 3, 4), *PV*: $n = 13$ neurons (3, 3, 4, 3), 4 mice). **j-k**, *VGLUT2*$^+$ ($n = 7$ mice) (**j**) or *PV*$^+$ ($n = 8$ mCh, $n = 9$ hM4Di mice) (**k**) inhibition. **l**, Recordings (*VGLUT2*: $n = 13$ (4, 5, 4), *PV*: $n = 12$ neurons (4, 3, 5), 3 mice). **m**, FISH. **n**, Anterograde tracing from $STN_{PV}$. **o**, *VGLUT3* FISH, *PV* antibody. 97.6% of *PV* expressed *VGLUT3* ($n = 3$ monkeys). **p**, 23.5% of *mCh* expressed *PV* ($n = 2$ monkeys). Mean ± SEM; $*P < 0.05$, $**P < 0.01$, $***P < 0.001$. One-way ANOVA, Bonferroni (**b**), paired *t* (**c**, **j**, **k**), unpaired *t* (**d-f**, **i**), two-way ANOVA, repeated, Bonferroni (**l**). Two-sided tests. $F = 6.47$, $P = 0.0007$, mCh vs. $PF_{CPu}$ $t = 3.04$, $PF_{CPu}$ vs. $PF_{STN}$ $t = 4.02$ (b), mCh $P < 0.0001$, $PF_{CPu}$ $P < 0.0001$, $PF_{STN}$ $P = 0.33$ (**c**), $P = 0.26$ (**d**), $P = 0.0012$ (**e**), $P = 0.043$ (**f**), $P < 0.0001$ (**i**), mCh $P = 0.012$, hM4Di $P = 0.022$ (**j**), mCh $P = 0.008$, hM4Di $P = 0.35$ (k), $F = 5.56$, DFn = 1, DFd = 161, $P = 0.03$ (**l**).

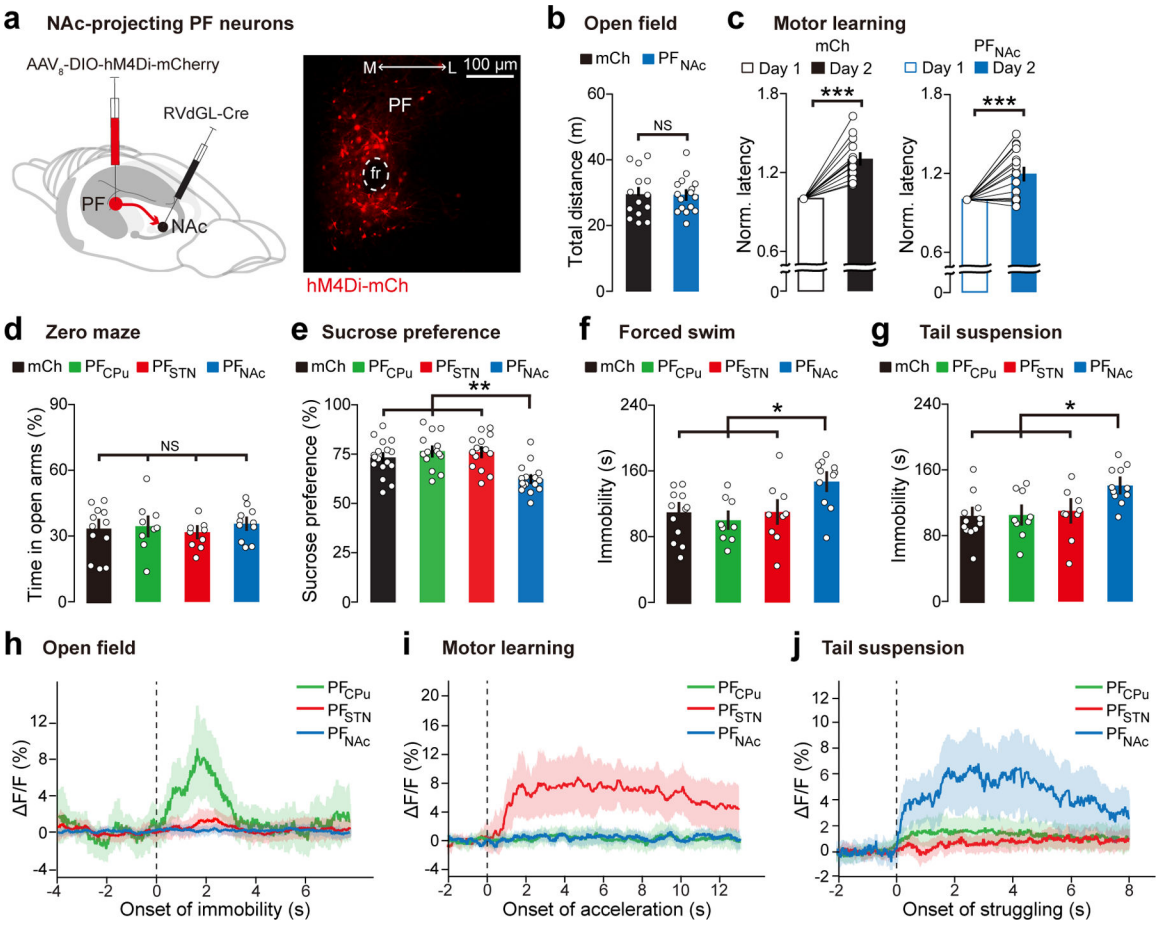


**Fig. 3. NAc-projecting PF neurons mediate depression-like behaviors.**

**a**, Inhibitory hM4Di expression in $PF_{NAc}$ neurons, by injecting retrograde RVdGL-Cre in NAc and Cre-dependent hM4Di-mCh in PF. **b-c**, Inhibition of $PF_{NAc}$ neurons during open field (**b**), rotarod (**c**) ($n$ = 14 mCh, $n$ = 16 $PF_{NAc}$ mice). mCh data from Fig. 2b, c. **d-g**, Inhibition of $PF_{CPu}$, $PF_{STN}$, or $PF_{NAc}$ neurons during zero maze (**d**), sucrose preference (**e**), forced swim (**f**), tail suspension (**g**) (**d**, **f**, **g**: $n$ = 12 mCh, $n$ = 9 $PF_{CPu}$, $n$ = 9 $PF_{STN}$, $n$ = 11 $PF_{NAc}$ mice; **e**: $n$ = 17 mCh, $n$ = 14 $PF_{CPu}$, $n$ = 14 $PF_{STN}$, $n$ = 16 $PF_{NAc}$ mice). **h-j**, *In vivo* fiber photometry recordings from $PF_{CPu}$, $PF_{STN}$, or $PF_{NAc}$ neurons by injecting a retrograde AAV expressing Cre in CPu, STN, or NAc, and Cre-dependent GCaMP6s in PF ($n$ = 5 mice per group). Fluorescence change aligned to the onset (0 s) of immobility during open field (**h**), to the onset of acceleration of the rod during rotarod (**i**), to the onset of struggling during tail suspension (**j**). Mean ± SEM; $*P < 0.05$, $**P < 0.01$, $***P < 0.001$. Unpaired $t$ (**b**), paired $t$ (**c**), one-way ANOVA, Bonferroni (**d-g**). Two-sided tests. $P = 0.94$ (**b**), mCh $P <$ 0.0001, $PF_{NAc}$ $P = 0.0005$ (**c**), $F = 0.55$, $P = 0.65$ (**d**), $F = 9.30$, $P < 0.0001$, mCh vs. $PF_{NAc}$ $t = 3.66$, $PF_{CPu}$ vs. $PF_{NAc}$ $t = 4.53$, $PF_{STN}$ vs. $PF_{NAc}$ $t = 4.41$ (**e**), $F = 5.04$, $P = 0.005$, mCh vs. $PF_{NAc}$ $t = 3.09$, $PF_{CPu}$ vs. $PF_{NAc}$ $t = 3.41$, $PF_{STN}$ vs. $PF_{NAc}$ $t = 2.79$ (**f**), $F = 5.20$, $P =$ 0.0042, mCh vs. $PF_{NAc}$ $t = 3.56$, $PF_{CPu}$ vs. $PF_{NAc}$ $t = 2.97$, $PF_{STN}$ vs. $PF_{NAc}$ $t = 2.87$ (**g**).

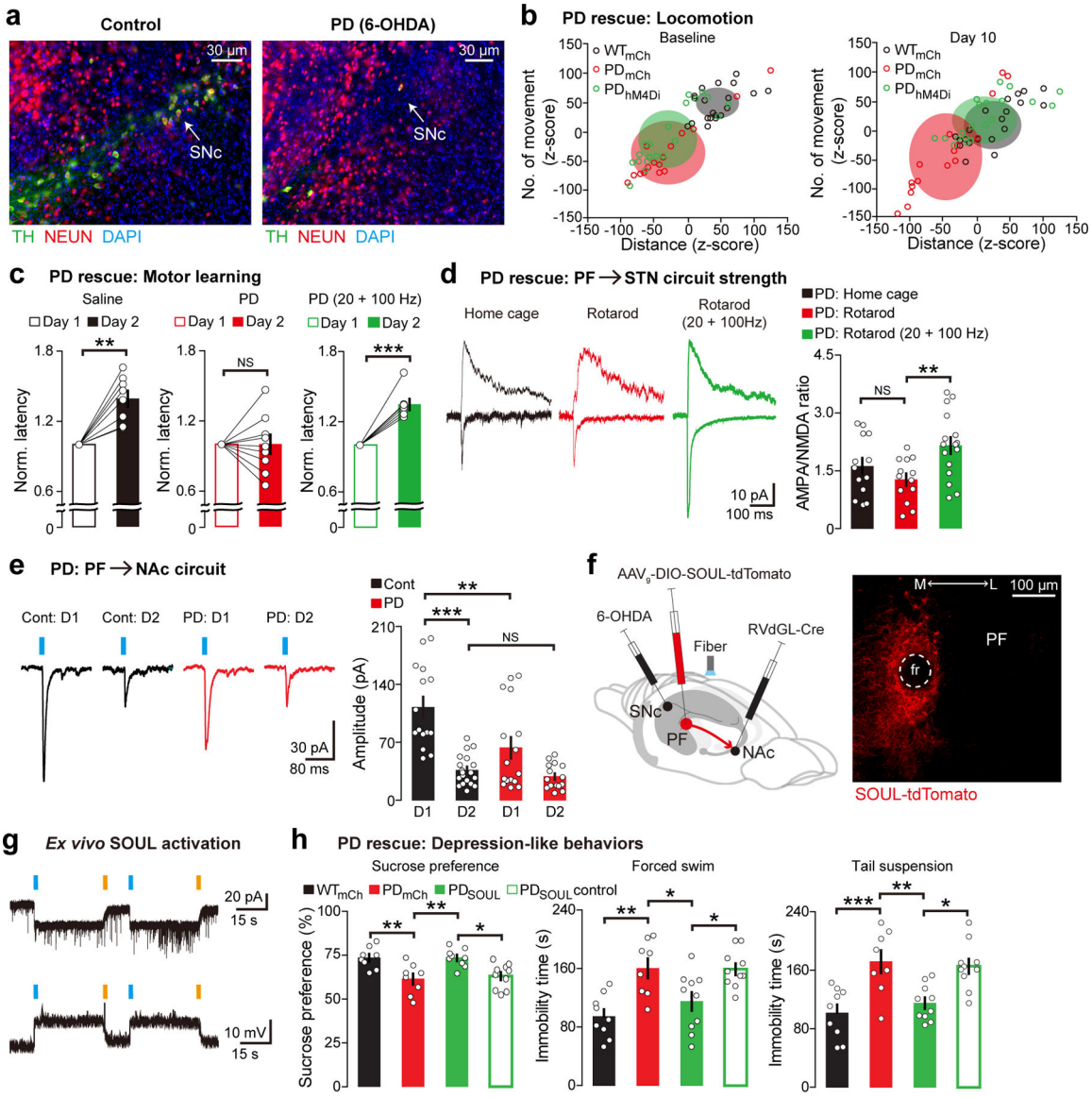


**Fig. 4. Targeting PF rescues motor deficits and depression-like behaviors in PD mice.**

**a**, Staining. **b**, $PF_{CPu}$ inhibition ($n$ = 20 $WT_{mCh}$, 16 $PD_{mCh}$, 20 $PD_{hM4Di}$ mice). **c**, PF→STN activation ($n$ = 8 saline, 9 PD, 7 PD/20+100 Hz mice). **d**, Recordings (Home: $n$ = 13 neurons (4, 4, 5), Rotarod: 13 (5, 4, 4), Rotarod (20+100 Hz): 16 (5, 5, 6), 3 mice). **e**, EPSCs in control (*D1*: $n$ = 15 neurons (3, 3, 4, 2, 3), *D2*: 19 (5, 4, 3, 4, 3), 5 mice), PD (*D1*: $n$ = 16 neurons (4, 3, 4, 3, 2), *D2*: 15 (3, 3, 3, 3, 3), 5 mice). **f**, PF→NAc manipulation. **g**, Current/voltage traces from a $PF_{NAc}$ neuron. **h**, $PF_{NAc}$ stimulation, sucrose ($n$ = 8 $WT_{mCh}$, 8 $PD_{mCh}$, 9 $PD_{SOUL}$, 10 $PD_{SOUL}$ control mice), forced/tail ($n$ = 9 $WT_{mCh}$, 8 $PD_{mCh}$, 10 $PD_{SOUL}$, 10 $PD_{SOUL}$ control mice). Mean ± SEM; *$P$ < 0.05, **$P$ < 0.01, ***$P$ < 0.001. Paired $t$ (**c**), one-way ANOVA, Bonferroni (**d**, **e**, **h**). Two-sided tests. Saline $P$= 0.0007, PD $P$= 0.98, PD (20+100 Hz) $P$= 0.0003 (**c**), $F$= 5.07, $P$= 0.011, Home vs. Rotarod $t$= 1.18, Rotarod vs. Rotarod (20+100 Hz) $t$= 3.14 (**d**), $F$= 16.24, $P$ < 0.0001, Cont *D1* vs. PD *D1* $t$= 3.67, Cont *D1* vs. Cont *D2* $t$= 5.95, Cont *D2* vs. PD *D2* $t$= 0.60 (**e**), Sucrose: $F$= 7.72,

$P$= 0.0005, $WT_{mCh}$ vs. $PD_{mCh}$ $t$= 3.50, $PD_{mCh}$ vs. $PD_{SOUL}$ $t$= 3.61, $PD_{SOUL}$ vs. $PD_{SOUL}$ control $t$= 3.29, Forced: $F$= 8.67, $P$= 0.0002, $WT_{mCh}$ vs. $PD_{mCh}$ $t$= 4.04, $PD_{mCh}$ vs. $PD_{SOUL}$ $t$= 2.84, $PD_{SOUL}$ vs. $PD_{SOUL}$ control $t$= 2.93, Tail: $F$= 9.87, $P$ < 0.0001, $WT_{mCh}$ vs. $PD_{mCh}$ $t$= 4.28, $PD_{mCh}$ vs. $PD_{SOUL}$ $t$= 3.54, $PD_{SOUL}$ vs. $PD_{SOUL}$ control $t$= 3.33 (**h**).

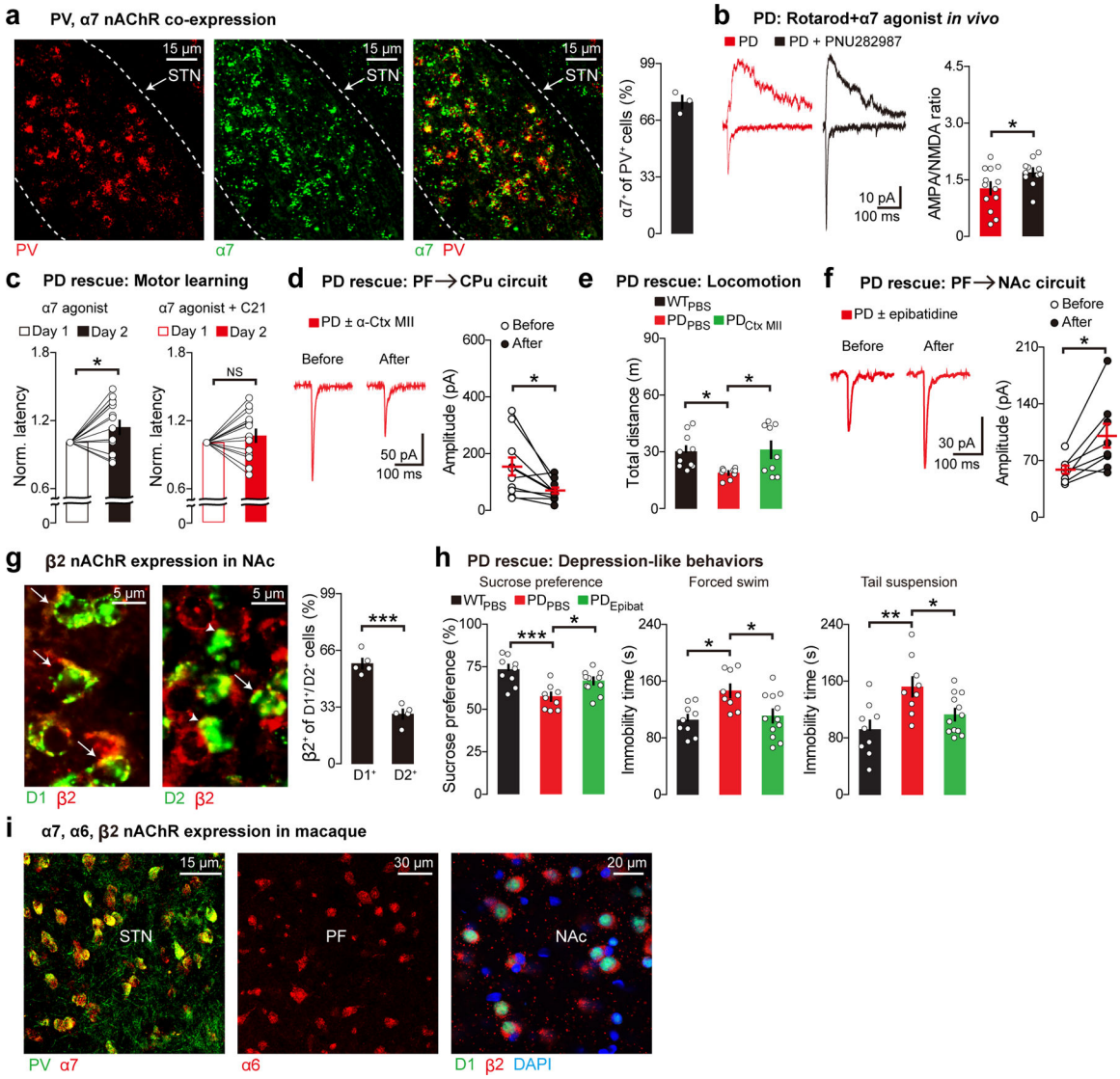


**Fig. 5. Modulating nAChRs in PF circuits rescues PD phenotypes.**

**a**, *PV*, *α7* FISH ($n = 3$ mice). **b**, Recordings (PD from Fig. 4d, PD + PNU282987: $n = 11$ neurons (4, 4, 3), 3 mice). **c**, Activating *α7* with $STN_{PV}$ inhibition ($n = 15$ mice). **d**, EPSCs from CPu ($n = 10$ neurons (2, 2, 2, 2, 2), 5 mice). **e**, α-Ctx MII infusion (1 μl) into CPu ($n = 10$ $WT_{PBS}$, $n = 9$ $PD_{PBS}$, $n = 9$ $PD_{Ctx\ MII}$ mice). **f**, EPSCs from *D1* in NAc ($n = 8$ neurons (2, 2, 2, 1, 1), 5 mice). **g**, *β2* with *D1*/*D2* FISH ($n = 5$ mice). **h**, Epibatidine infusion (250 nl) into NAc, sucrose ($n = 9$ $WT_{PBS}$, $n = 9$ $PD_{PBS}$, $n = 11$ $PD_{Epibat}$ mice), forced ($n = 9$ $WT_{PBS}$, $n = 9$ $PD_{PBS}$, $n = 12$ $PD_{Epibat}$ mice), tail ($n = 9$ $WT_{PBS}$, $n = 9$ $PD_{PBS}$, $n = 12$ $PD_{Epibat}$ mice). **i**, *PV* antibody, *α7*, *α6*, *β2*, *D1* FISH. DAPI (blue). Mean ± SEM; $*P < 0.05$, $**P < 0.01$, $***P < 0.001$. Unpaired *t* (**b**, **g**), paired *t* (**c**, **d**, **f**), one-way ANOVA, Bonferroni (**e**, **h**). Two-sided tests. $P = 0.042$ (**b**), agonist $P = 0.035$, agonist + C21 $P = 0.27$ (**c**), $P = 0.018$ (**d**), $F = 4.91$, $P = 0.016$, $WT_{PBS}$ vs. $PD_{PBS}$ $t = 2.64$, $PD_{PBS}$ vs. $PD_{Ctx\ MII}$ $t = 2.80$ (**e**), $P = 0.012$ (**f**), $P < 0.0001$ (**g**), Sucrose: $F = 10.53$, $P = 0.0004$, $WT_{PBS}$ vs. $PD_{PBS}$ $t = 4.57$, $PD_{PBS}$ vs. $PD_{Epibat}$ $t = 2.79$, Forced: $F = 6.19$, $P = 0.0061$, $WT_{PBS}$ vs. $PD_{PBS}$ $t = 3.20$,

$PD_{PBS}$ vs. $PD_{Epibat}$ $t = 2.95$, Tail: $F = 7.00$, $P = 0.0035$, $WT_{PBS}$ vs. $PD_{PBS}$ $t = 3.68$, $PD_{PBS}$ vs. $PD_{Epibat}$ $t = 2.56$ (**h**).